



UNIVERSITY OF LEEDS

This is a repository copy of *Temperature and Pressure Studies of the Reactions of CH₃O₂, HO₂, and 1,2-C₄H₉O₂ with NO₂*.

White Rose Research Online URL for this paper:
<http://eprints.whiterose.ac.uk/91542/>

Version: Accepted Version

Article:

McKee, K, Blitz, MA and Pilling, MJ (2016) Temperature and Pressure Studies of the Reactions of CH₃O₂, HO₂, and 1,2-C₄H₉O₂ with NO₂. *Journal of Physical Chemistry A*, 120 (9). pp. 1408-1420. ISSN 1089-5639

<https://doi.org/10.1021/acs.jpca.5b06306>

Reuse

Unless indicated otherwise, fulltext items are protected by copyright with all rights reserved. The copyright exception in section 29 of the Copyright, Designs and Patents Act 1988 allows the making of a single copy solely for the purpose of non-commercial research or private study within the limits of fair dealing. The publisher or other rights-holder may allow further reproduction and re-use of this version - refer to the White Rose Research Online record for this item. Where records identify the publisher as the copyright holder, users can verify any specific terms of use on the publisher's website.

Takedown

If you consider content in White Rose Research Online to be in breach of UK law, please notify us by emailing eprints@whiterose.ac.uk including the URL of the record and the reason for the withdrawal request.



eprints@whiterose.ac.uk
<https://eprints.whiterose.ac.uk/>

Temperature and Pressure Studies of the Reactions of CH_3O_2 , HO_2 and 1-,2- $\text{C}_4\text{H}_9\text{O}_2$ with NO_2

Kenneth McKee^a Mark A. Blitz,^{a,b*} and Michael J. Pilling^a

^a School of Chemistry, University of Leeds, Leeds, LS2 9JT, UK

^b National Centre for Atmospheric Science, University of Leeds, Leeds, LS2 9JT, UK

*E-mail: m.blitz@leeds.ac.uk

ABSTRACT

A novel technique has been developed for the detection of peroxy radicals in order to study their kinetics with NO_2 . Peroxy radicals (RO_2 , where $\text{R} = \text{H}$, CH_3 and 1-,2- C_4H_9) were produced by laser flash photolysis and were probed by photo-dissociation of the RO_2 and the subsequent detection of either OH or CH_3O photo-fragments by laser induced fluorescence. Reaction (1), $\text{CH}_3\text{O}_2 + \text{NO}_2 + \text{M} \rightleftharpoons \text{CH}_3\text{O}_2\text{NO}_2 + \text{M}$ ($\text{M} = \text{N}_2$), was studied between 25-400 Torr at 295K giving results in excellent agreement with the literature. At temperatures between 333 - 363 K equilibration was observed and yielded $\Delta_r H^\circ_{298}(1) = -93.5 \pm 0.3 \text{ kJ mol}^{-1}$. Reaction (2), $\text{HO}_2 + \text{NO}_2 + \text{M} \rightleftharpoons \text{HO}_2\text{NO}_2 + \text{M}$ ($\text{M} = \text{N}_2$), was studied at 295 K and showed kinetics in fair agreement with the literature. Equilibration at higher temperatures was obscured by an additional loss of HO_2NO_2 from the system. In addition, the OH quantum yield from photolysis of HO_2NO_2 at 248nm

was determined to be 0.15 ± 0.03 . Reaction (3), $1,2\text{-C}_4\text{H}_9\text{O}_2 + \text{NO}_2 + \text{M} \rightleftharpoons 1,2\text{-C}_4\text{H}_9\text{O}_2\text{NO}_2 + \text{M}$ ($\text{M} = \text{He}$), was studied between 241 – 341 K and at the higher temperatures equilibration was observed, which yielded $\Delta_r H_{298}^\circ(3) = -93.5 \pm 0.6 \text{ kJ mol}^{-1}$. The low uncertainties in the enthalpies of formation for both CH_3O_2 and $1,2\text{-C}_4\text{H}_9\text{O}_2$ are a result of using a master equation method that allows global analysis of all the available rate data (present measurements and literature values) for forward and reverse reactions under all conditions of temperature and pressure.

Introduction

Peroxy species are important intermediates in the oxidation of volatile organic compounds (VOC) in the atmosphere and combustion systems. In polluted atmospheres, the reaction with NO_x to form peroxy nitrates becomes an important factor in the eventual fate of the RO_x species. If the RO_2NO_2 lifetime is long enough they may act either as a sink, transporting NO_x , or may react with OH, effectively removing HO_2 radicals. The atmospheric lifetime of peroxy nitrates is dependent on their thermal stability, photo-stability and their rates of reaction with reactive species such as OH and via heterogeneous reactions. For instance peroxyacetyl nitrate (PAN) can have a long enough lifetime in the troposphere to allow transport from polluted to clean air.¹⁻² The RO_2NO_2 species studied here are less stable than PAN but they play a significant role in the speciation of NO_y .

Accurate kinetic, thermodynamic, and photochemical data are needed to predict the effect of peroxyxynitrate species on NO_x, OH and O₃ concentrations. Due to the inherent instability of RO₂NO₂ species at room temperature and the difficulty in isolating them, it is hard to gain accurate thermodynamic information.



Early studies of (1) by Sander and Watson³ and Ravishankara et al.⁴ used UV-Vis absorption to detect CH₃O₂. Both of these studies gave similar results of $k_1^\infty = 7.0 \times 10^{-12} \text{ cm}^3 \text{ molecule}^{-1} \text{ s}^{-1}$ and $k_1^0 = 2.2 \times 10^{-30} \text{ cm}^6 \text{ molecules}^{-2} \text{ s}^{-1}$ at 298K. Ravishankara et al. also varied the temperature but no reverse reaction was observed even at 353K. Bridier et al.⁵ also studied reaction (1) using UV-Vis absorption to detect CH₃O₂ over the temperature range 333-373K. The approach to equilibrium was observed and analysis gave $\Delta_r H_{298}^\circ(1) = -92 \text{ kJ mol}^{-1}$. More recently Wallington et al.⁶ completed a high pressure study, using an SF₆ bath gas with UV-Vis detection of CH₃O₂, which resulted in a much higher k_1^∞ of $1.8 \times 10^{-11} \text{ cm}^3 \text{ molecule}^{-1} \text{ s}^{-1}$

Zabel et al.⁷ have studied reaction (-1) using FTIR spectrometry to observe the decay of CH₃O₂NO₂ over the temperature range 245 - 273K. These data, combined with the information on the forward reaction by Sander et al.³ and Ravishankara et al.,⁴ were used to calculate an enthalpy of dissociation of 92 kJmol⁻¹. The thermal lifetime of CH₃O₂NO₂ at the tropopause was estimated to be 12 days.



Reaction (2) is one of the most widely studied $\text{RO}_2 + \text{NO}_2$ reactions.^{2, 8-15} Until 2000 the most widely accepted results were the determinations by Kurylo and Ouellette.¹⁶⁻¹⁷ They measured the pressure and temperature dependence of the reaction over the range 25 - 600 Torr of N_2 , O_2 and temperatures between 228 –353K. These studies probed HO_2 by UV-Vis spectroscopy. Values of $k_2^\infty = 4.7 \times 10^{-12} \text{ cm}^3 \text{ molecule}^{-1} \text{ s}^{-1}$ and $k_1^0 = 1.8 \times 10^{-31} \text{ cm}^6 \text{ molecule}^{-2} \text{ s}^{-1}$ were obtained for the forward reaction. Very little difference was observed between O_2 and N_2 as a third body. More recently there have been two studies by Christensen et al.¹⁸ and Bacak et al.¹⁹ who used more precise experiments to explore the reaction over an even larger temperature and pressure range, where Bacak et al. observed a significantly lower rate coefficient at 200 K.

The reverse reaction has also been studied, most recently by Zabel²⁰ at low temperatures (<292K) using FTIR detection of HO_2NO_2 (Perinitric acid or PNA). These results were combined with the data of Kurylo and Ouellette¹⁷ obtaining $\Delta_r H_{298}^\ominus(2) = -99.6 \pm 3.1 \text{ kJ mol}^{-1}$. A recent study by Gierczak et al.²¹ observed equilibrium between 331 and 350 K and determined $\Delta_r H_{298}^\ominus(2) = -100.4 \pm 2.1$.

Also relevant to this study is the work on the photolysis of PNA at 248nm by Macleod et al.²² and Roehl et al.²³ Both studies used the photolysis of a synthetic sample of PNA and detected the photolysis product by LIF. MacLeod et al. observed OH production obtaining $\phi_{\text{OH,PNA}} = 0.34 \pm 0.16$ and also suggested that OH was formed vibrationally and rotationally cold. Roehl et al.²³ carried out a similar study which looked at NO_2 fluorescence and found $\phi_{\text{NO}_2,\text{PNA}} = 0.56 \pm 0.17$. More recently Jimenez

et al.²⁴ measured both $\phi_{\text{OH,PNA}}$ (0.09) and $\phi_{\text{HO}_2,\text{PNA}}$ (0.89), which questioned the validity of the measurements of Macleod et al.²²



No studies have been carried out into the kinetics of the forward reaction, but measurements have been made for $(\text{CH}_3)_3\text{CO}_2$.²⁵ As with the other RO_2NO_2 molecules in this study Zabel et al.⁷ has measured its decomposition kinetics.

Most previous studies used UV-Vis spectroscopy as a detection method for peroxy species. A significant flaw is that the products and reactants have overlapping spectra so that corrections have to be made to the spectral time profiles to extract kinetics. The more recent studies by Christensen et al.¹⁸ and Bacak et al.¹⁹ overcame this difficulty by using near infra-red (NIR) and mass spectroscopies to monitor RO_2 kinetics. In the present study we apply another technique to study RO_2 kinetics: RO_2 radical photolysis at 248 nm, to generate either OH or CH_3O , followed by probing the photo-fragment with laser induced fluorescence before any subsequent chemistry can occur. Detection of peroxy radicals in the near-infrared is possible using cavity ring down spectroscopy but their small absorption cross-sections for $\text{R} \neq \text{H}$ means that this method is relatively insensitive, and hence only the kinetics of peroxy self-reactions have been reported.²⁶

In this paper we report kinetics on the reaction of RO_2 ($\text{R}=\text{H}, \text{CH}_3, \text{C}_4\text{H}_9$) + NO_2 where the temperature was tuned over a range where the approach to equilibrium was observed. Master equation analysis using MESMER²⁷ was then used to fit the kinetic data, together with the literature data, in order to assess the kinetics and to best define

the thermodynamics of the reaction. For $R = \text{CH}_3$ and C_4H_9 the kinetics are straightforward and there is good agreement with the literature. However, for $R = \text{H}$ the kinetics are more complicated because interferences occur.

METHODS

Experimental

The experimental technique consists of laser flash photolysis (LFP) coupled with time resolved laser induced fluorescence (LIF); the system similar to one previously described,²⁸⁻²⁹ except for the addition of a second photolysis laser, which fires approximately 100-200 ns before the probe laser. This second photolysis laser photodissociates the peroxy radical to generate either OH or CH_3O , which is then detected by the probe (LIF) laser. The time delay between the second photolysis laser and the probe is short enough such that no chemistry can occur, so that the detected signal provides a measure of the RO_2 radical concentration at a delay time defined by the second photolysis laser.

The set-up consisted of a six way stainless steel cross, with the time-zero photolysis and probe lasers at right-angles and with their beams overlapping in the centre of the cell. Fluorescence was detected perpendicularly to the plane defined by the lasers. The time-zero photolysis laser was either a 248 nm or 351 nm (Lambda Physik, LPX105) excimer outputting ca. 150mJ / pulses. The second photolysis excimer laser (Lambda Physik, MINEX, 10-25 mJ/pulse at 248 nm) was at right angles to the time-

zero laser and its beam counter-propagated that from the Nd-YAG pumped dye laser (Spectron, SL803 / SL4000, ~3mJ/pulse) that excited the LIF at 282 or 298.5 nm. These wavelengths were generated by doubling the dye laser output at 564 nm (Rhodamine 6G) and 597 nm (Rhodamine B) using a KDP doubling crystal and were used to probe OH and CH₃O, respectively. The lower intensity of the MINEX excimer laser was increased by focusing with a 70 cm focal length lens, which was positioned 40 – 60 cm away from the centre of the cell. To check this focusing had no effect on the kinetics, traces were taken with and without the lens at distances 10-60 cm away from the cell. Comparison of these traces returned the same kinetics.

The OH($A^2\Sigma^+ - X^2\Pi$) and CH₃O ($A^2A_1 - X^2E$) bands were excited by 282 nm and 298.5 nm light, respectively. The fluorescence signal was collected and filtered before being detected with a photomultiplier (Electron Tubes QKB9813); a 310nm interference filter (Corion) and a 350nm cut-off filter (Schott BG7) were used for the detection of OH and CH₃O, respectively. The collection optics consisted of two plano-convex lenses, focal length 4cm, located inside the reaction cell. A Stanford Research Systems SR250 boxcar was used to integrate the PMT signal, which was subsequently outputted to a home built analogue to digital converter before being stored on a Personal Computer for further processing. The firing of the lasers was controlled by a home built timer card, which fired the time-zero laser and scanned the LIF laser over 100 time points, where each time point was the average of between 4 -12 laser samples. The second photolysis laser was fired between 100 – 200 ns before the LIF laser. This time difference was set using the variable time output of the Spectron laser, which was synchronized with respect to the Q-switch.

For experiments above 295K, the cell was heated by 4 cartridge heaters, which allowed the temperature to be controlled to ± 2 K. The low temperature study was carried out using a reaction cell surrounded by a methanol bath. The methanol was cooled by a low temperature element, Labplant RP-100, which controlled the temperature to ± 2 K. Gas flows were controlled by MKS (1160 and 1159) and Tylan (FC280 and FC260) mass flow controllers, which were calibrated against bubble flow meters.

Generation of RO₂ Species

HO₂

Oxalyl chloride was used as a chlorine radical source, and in the presence of CH₃OH and O₂, HO₂ was produced by the following well-known reaction scheme:



The photolysis of oxalyl chloride at 248nm produces Cl via two pathways:



A recent study by Gosh et al.³⁰ has shown that P1a/(P1a+P1b) is equal to 0.79 ± 0.15 at 248 nm, but the reaction



is sufficiently fast (microseconds), that the yield of Cl from oxalyl chloride is essentially 2. Typical gas concentrations for the HO₂ experiments were: 5 Torr oxygen, 30 - 50 mTorr of oxalyl chloride, 100 - 300 mTorr of methanol and 0 - 40 mTorr of NO₂. Concentrations of HO₂ were typically less than 1×10^{13} molecule cm⁻³.

Under these experimental conditions all HO₂ was produced within 3 μs of the initial photolysis pulse. Nitrogen was used as the buffer gas for the kinetic experiments and 400 Torr of helium was used while investigating equilibrium at the higher temperatures.

CH₃O₂



248nm photolysis of methyl iodide was used for the production of CH₃ radicals which, in the presence of excess O₂, produces CH₃O₂. In order to keep the rate of reaction (8) fast enough to ensure most of the CH₃ reacted with O₂, concentrations of O₂ had to be kept at about 10 Torr regardless of the bath gas pressure. Even at 25 Torr total pressure the lifetime of CH₃, 19μs, is far shorter than the time scale of the experiments. Nitrogen was used as the buffer gas.

C₄H₉O₂

The following scheme was used to generate C₄H₉O₂ radicals from n-butane:



Reaction 9 produces both 1-C₄H₉ and 2-C₄H₉ alkyl radicals, therefore any kinetics obtained are for a mixture of both 1-C₄H₉O₂ and 2-C₄H₉O₂ radicals. Tyndall et al.³¹ studied the partitioning between the two isomers in reaction 9 and found a ratio for production of 1-C₄H₉ to 2-C₄H₉ of 0.3:1.0. The majority of the kinetics measured was

therefore due to 2-C₄H₉O₂. For the C₄H₉O₂ experiments typical gas concentration were: 12 - 20 mTorr of Cl₂, 300 - 400 mTorr of O₂, 0 - 30 mTorr of NO₂ and 80-100 mTorr of n-C₄H₁₀. Helium was used as the buffer gas.

Oxygen, nitrogen and helium were CP grade (BOC, 99.999%), methanol (Analar grade), chlorine was 5% in helium (BOC), oxalyl chloride was 99% purity (Avocado Research), methyl iodide was 99% purity (Aldrich) and n-butane was Meiser Griesheim, 99.95%.

Master Equation Analysis

A major aim of this paper is the determination of the pressure dependence of the forward and reverse rate coefficients, k_{bim} and k_{rev} and the enthalpy of reaction for reactions of the type:



We employ a master equation analysis using the code MESMER.^{27, 32} The application of the master equation to reactions in the gas phase has been extensively discussed elsewhere.³²⁻³⁶ Here, the main points are summarized and the manipulations required to accommodate second order systems are discussed. Typically the energy spaces of the species involved in a reaction are partitioned into a number of contiguous intervals or grains that are assigned values for the numbers of states they contain, average energies, and, where appropriate, average values of microcanonical rate coefficients. These grains form the basis of the master equation representation of the system, an equation of motion of the grain probabilities, which is usually represented as,

$$\frac{d\mathbf{p}}{dt} = \mathbf{M} \mathbf{p}$$

where \mathbf{p} is a vector containing the probability densities of the populations of the grains and the matrix \mathbf{M} contains the transition rates between the grains either because of collisional activation/deactivation or because of reaction. The evolution of \mathbf{p} is limited by two constraints, mass (or density) conservation and detailed balance.

The solution to Eq. (1) can in general be written as,

$$\mathbf{p} = \mathbf{U} e^{\mathbf{\Lambda} t} \mathbf{U}^{-1} \mathbf{p}_0$$

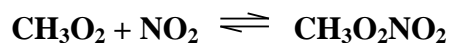
where $\mathbf{\Lambda}$ is a diagonal matrix containing the eigenvalues of \mathbf{M} , \mathbf{U} is a matrix of the corresponding eigenvectors and \mathbf{p}_0 is a vector containing the initial grain population densities. The number of eigenvalues is equal to the total number of grains; all the eigenvalues are negative. They can be divided into two types, internal energy relaxation eigenvalues (IEREs), which relate to the collisional relaxation of the internal energy of the system and chemically significant eigenvalues (CSEs); the magnitudes of the reciprocal CSEs relate to the timescales of the chemical reactions and the number of CSEs is related to the number of chemical species included in the master equation. Generally, and certainly in the reactions analysed here, the CSEs are significantly smaller in magnitude than the IEREs – energy relaxation occurs on timescales that are shorter than those of chemical reaction. Under these circumstances, the rate coefficients for the chemical reactions can be determined from an analysis of the eigenvalues and eigenvectors of the CSEs. In the present system, there are two CSEs, one of which, λ_1 , relates to the establishment of equilibrium and is zero. The non-zero eigenvalue, $\lambda_2 = - (k_{\text{bim}}[\text{NO}_2] + k_{\text{rev}})$, and $K_{\text{eq}} = k_{\text{bim}}/ k_{\text{rev}}$.

MESMER includes a facility which allows pressure and temperature dependent forward and reverse rate coefficients to be fitted to a reaction model. The molecular constants for the reactants and product are fed into the model and are listed in the Supporting Information. The limiting high-pressure rate coefficient for association, k_{bim}^{∞} , is parameterised as $A(T/298 \text{ K})^n$ and the microcanonical rate constants for dissociation of RO_2NO_2^* , $k(E)$ are determined by inverse Laplace transformation.³⁷ The rates of reaction from $\text{RO}_2 + \text{NO}_2$ into a particular grain of RO_2NO_2 are determined by detailed balance.³⁸ An exponential down model, coupled with detailed balance, is used for the probabilities of collisional energy transfer between the grains, based on the parameterization $\langle \Delta E \rangle_{\text{down}} = \langle \Delta E \rangle_{\text{down},298} (T/298 \text{ K})^m$.³⁹ All of the available data were fitted to the master equation model, using the minimization of χ^2 :

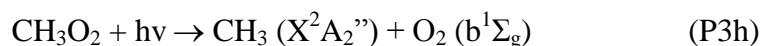
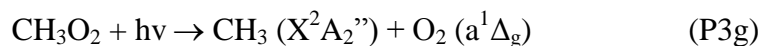
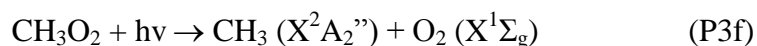
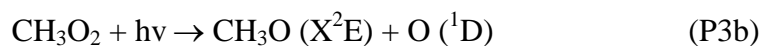
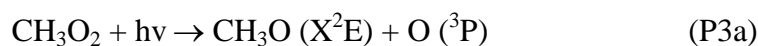
$$\chi^2 = \sum_{i=1}^N (k_{i,\text{exp}} - k_{i,\text{model}})^2 / \sigma_i^2$$

as the criterion of best fit. Here $k_{i,\text{exp}}$ is the i th experimental rate coefficient, $k_{i,\text{model}}$ is the model result under the same conditions of T and p , σ_i is the standard deviation of the experimental rate coefficient and N is the total number of experimental measurements. The analysis was conducted, as were the experiments, under pseudo first order conditions ($[\text{NO}_2] \gg [\text{RO}_2]$). The bimolecular forward rate constant, k_{bim} was used in the fits and $[\text{NO}_2]$ was given a fixed value of $10^{15} \text{ molecule cm}^{-3}$). The variable parameters in the fitting process were $\Delta_r H^{\circ}_0$, A , n , $\langle \Delta E \rangle_{\text{down},298}$ and m . The best available experimental data (literature values of the forward and reverse rate coefficients and the values determined here, including measurements of rate coefficients made under equilibrating conditions) were used in a global fit for $R = \text{CH}_3$ and 1-,2- C_4H_9 (see below).

Results and Discussion



The products of the 248 nm photolysis of CH_3O_2 have not been fully characterised and many products are energetically possible:



Although the complete product distribution is not known at 248 nm, the quantum yields for OH and CH_3O have been measured by Hartmann et al.⁴⁰ to be $\phi_{\text{OH}} = 0.06$ and $\phi_{\text{CH}_3\text{O}} = 0.20$. They found that methoxy radicals, CH_3O , are only formed in the ground state and suggested that OH was formed by isomerisation of CH_3O_2 to CH_2OOH , followed by cleavage of the O-O bond. If this is the case then larger alkylperoxy species might also be expected to have an OH channel, (see section on $\text{C}_4\text{H}_9\text{O}_2$). Therefore our observation of fluorescence from CH_3O is consistent with Hartmann et al.⁴⁰ and implies our technique is a sensitive probe for methyl peroxy.

Pressure dependence at room temperature

The reaction was studied at room temperature over the pressure range 25 –400 Torr, using N₂ as the bath gas. The experimental conditions of this study, [CH₃O₂] << [NO₂], mean pseudo-first order kinetics were observed, and an example of a kinetic trace is shown in Figure 1. As noted in the experimental ≥ 10 Torr of O₂ was added to the system to ensure that reaction 8 was fast. This effectively suppresses the formation of CH₃O from the radical-radical reaction:⁴¹



However, when NO₂ is added to the system CH₃O can be formed from the reaction:⁴²



and the amount of CH₃O will increase as more NO₂ is added. However, under all conditions [CH₃O₂] > [CH₃O] and therefore the kinetics from reaction 1 will be little affected. However, the viability of the detection technique may be compromised. The method used to monitor CH₃O₂ involves photolysis and then the use of CH₃O as a proxy for CH₃O₂, using LIF detection. The CH₃O LIF signal will be affected by the occurrence of reaction 12 which leads to the formation of a small amount of CH₃O in the system which may be comparable to the small fraction of the CH₃O₂ that is photolysed to CH₃O. A rough estimate indicates that about > 10% of the CH₃O₂ is photolysed to CH₃O, based on $\sigma_{\text{CH}_3\text{O}_2,248\text{nm}} \sim 5 \times 10^{-18} \text{ cm}^{-2}$ ⁴³ and a photon intensity of 10¹⁷ photon cm⁻². In practice it was found that the three-laser CH₃O signal was always significantly larger than the signal from just two-lasers (initial photolysis + LIF detection laser). Subtracting the two-laser signal from the three-laser experiment yields a signal that is a proxy for CH₃O₂ alone and allows its kinetics to be determined. This procedure was followed throughout before kinetic analysis and leads to increased noise in the CH₃O₂ traces, see Figure 1. It is also noted that CH₃O is

more reactive than CH_3O_2 towards NO_2 therefore at longer times the three-laser signal is nearly exclusively due to CH_3O_2 .

The CH_3O_2 kinetic data were fitted to a single exponential:

$$[\text{CH}_3\text{O}_2] = [\text{CH}_3\text{O}_2]_0 \exp(-k_1' t) \quad (\text{E1})$$

where k_1' is the pseudo-first-order rate constant, $k_1' = k_1[\text{NO}_2]$. An example of the fit to the data is shown in Figure 1. $[\text{NO}_2]$ was varied up to 35 mTorr, and the bimolecular rate coefficient, k_1 , for the reaction was obtained from a plot of k_1' versus $[\text{NO}_2]$. An example of such a plot is shown in Figure 2, where the slope is equal to the bimolecular rate constant; the results are summarised in Table 1.

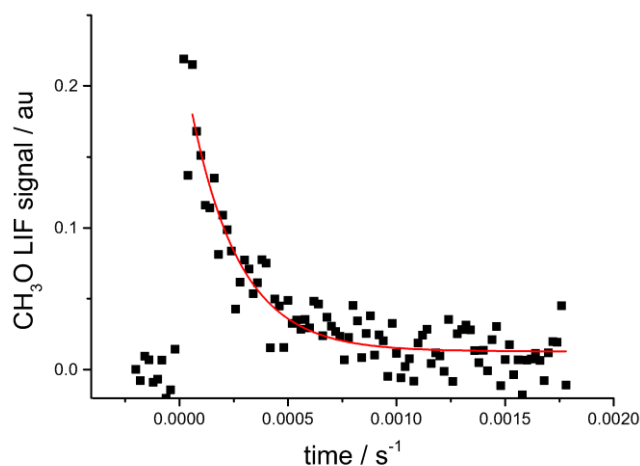


Figure 1. Kinetic trace for $\text{CH}_3\text{O}_2 + \text{NO}_2$ at 295 K and 32.1 mTorr of NO_2 at 400 Torr total pressure. The solid line is the best fit first-order decay, eq E1, to the data, where $k_1' = 4505 \pm 421 \text{ s}^{-1}$.

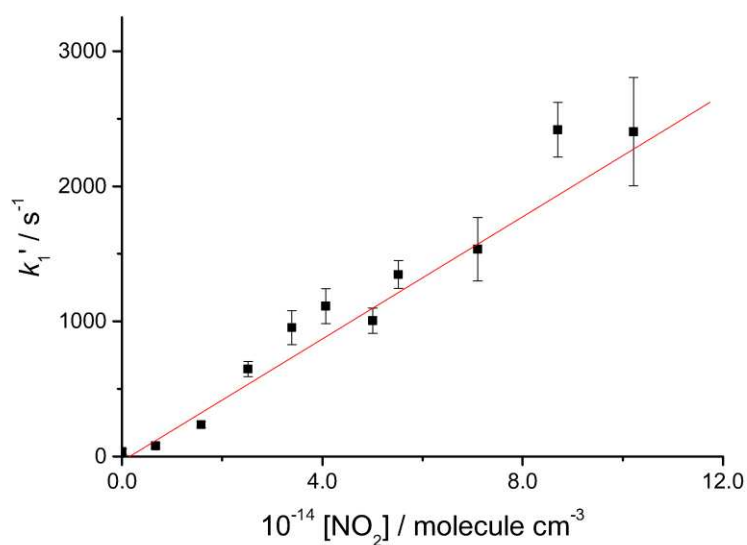


Figure 2. Bimolecular plot for the $\text{CH}_3\text{O}_2 + \text{NO}_2$ kinetic data at a total pressure of 51 Torr (N_2) and at 295 K.

Pressure /Torr	$10^{12} k_1 / \text{cm}^3 \text{ molecule}^{-1} \text{ s}^{-1}$
26	0.82 ± 0.08
51	1.15 ± 0.16
99	1.50 ± 0.14
230	2.26 ± 0.18
399	3.05 ± 0.24

Table 1. Values of the bimolecular rate constant for $\text{CH}_3\text{O}_2 + \text{NO}_2$ at 295 K, as a function of the pressure of the N_2 buffer gas. The errors are $\pm 2\sigma$, from the analysis of second order plots, c.f. Figure 2.

The results from Table 1 are plotted together with values from the literature in Figure 3. From this figure it can be concluded that the results from the study are in excellent agreement, confirming the validity of the current experimental method. Included in

Figure 3 is a master equation fit to the data, see below for further details, where the limiting high-pressure rate coefficient, k_1^∞ , is equal to $(8.8 \pm 2.5) \times 10^{-12} \text{ cm}^3 \text{ molecule}^{-1} \text{ s}^{-1}$, where the uncertainty is $\pm 2\sigma$. This result conflicts with the study of this reaction by Wallington et al.,⁶ where at 14 bar of SF_6 k_1 was measured to be $1.3 \pm 0.1 \times 10^{-11} \text{ cm}^3 \text{ s}^{-1}$. This conclusion is further supported by global master equation analysis of the literature data for association and dissociation, discussed below. The reason for the inconsistency in this study is not clear but it is more likely to be related to the experimental technique rather than an additional reaction channel operating at higher pressure.

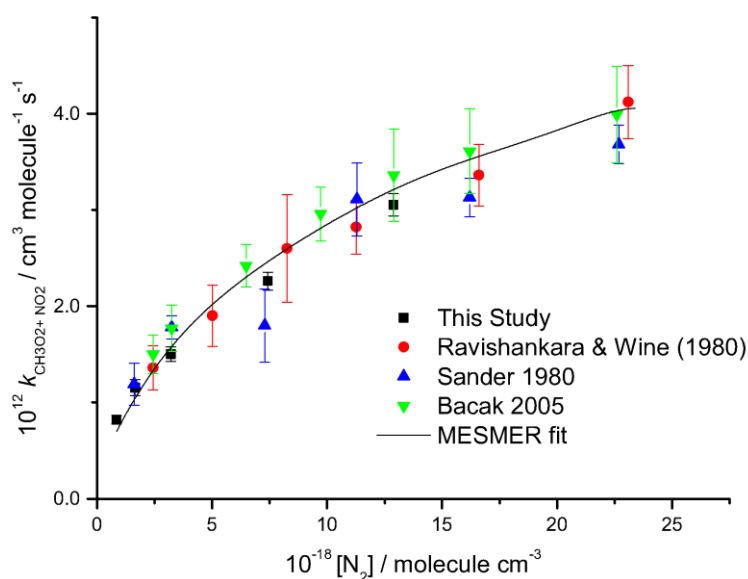


Figure 3. Plot of the pressure dependence of $\text{CH}_3\text{O}_2 + \text{NO}_2$ at 295 K from this study and the literature, where N_2 is the buffer gas: \blacksquare = this study; \bullet = Ravishankara et al.;⁴ \blacktriangle = Sander et al.;³ and \blacktriangledown = Bacak et al.⁴⁴ All errors are 2σ . The solid line is the MESMER fit to the data, see text below for details.

Temperature Dependence Studies

The equilibrium behaviour of this reaction was studied over the temperature range 333 K – 363 K at a total pressure of 400 Torr, N_2 . Equilibration was first observed

clearly at 333 K continuing up to 363K where little forward reaction could be observed. An example of the approach to equilibrium is shown in Figure 4. At least 8 traces with $0 < [\text{NO}_2] < 25\text{mtorr}$ were acquired at each temperature. Observation of equilibrium behaviour allows that thermodynamics of the reaction to be determined directly from the measured equilibrium constant.

The concentration profiles of $[\text{CH}_3\text{O}_2]$ are described by a biexponential function. The analytical expression for $[\text{CH}_3\text{O}_2](t)$ is given in the SI ($[\text{CH}_3\text{O}_2] = M2$), where for the present system $k_1' = k_1[\text{NO}_2] = k_{\text{bim}}[\text{NO}_2]$, $k_{-1} = k_{\text{rev}}$, and k_{diff1} and k_{diff2} are the slow diffusion of CH_3O_2 and $\text{CH}_3\text{O}_2\text{NO}_2$ out of the reaction zone. All the other parameters in the generic scheme in the SI were set to zero, i.e. $k_X = 0$. k_{diff1} was determined from the RO_2 kinetic trace with no added $[\text{NO}_2]$, and k_{diff2} was assigned using the dependence of the diffusion coefficient on mass, see the SI. The data fitting returns the rate coefficients k_1 and k_{-1} , which define the equilibrium constant for reaction (1): $K_c = k_1/k_{-1}$.

The pseudo first order conditions, $[\text{CH}_3\text{O}_2] \ll \text{NO}_2$, were maintained throughout the equilibration experiments. Retrieving defined multiple rate coefficients from a single kinetic trace is problematic. Therefore, to improve the reliability of returned rate coefficients, a global analysis⁴⁵ was carried using OriginPro 9.1.⁴⁶ Global analysis, i.e. the analysis of multiple temporal profiles under a range of NO_2 concentrations, significantly decreases the errors in the returned rate coefficients and provides a more rigorous test of the reaction mechanism. All the rate coefficients were treated as global and the signal height as local, and $[\text{NO}_2]$ was an extra independent variable that was required to define k_1' via $k_1[\text{NO}_2]$. Global analysis was carried out at each temperature. An example of the global fit to an individual kinetic trace is shown in

Figure 4 and the results are given in Table 2. From Table 2 it can be seen that the values of K_c are in excellent agreement with those of Bridier et al.,⁵ the only previous study that observed equilibrium in reaction 1. It is noted that in the study by Ravishankara⁴ experiments were carried out at 350 K and no equilibrium was observed. The reason for this failure to see equilibration is not apparent.

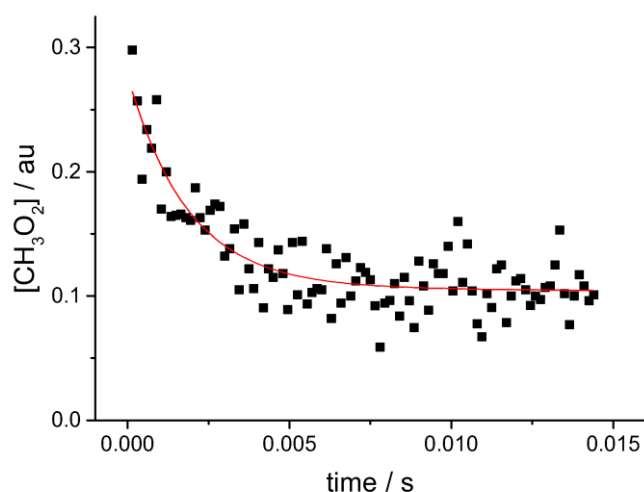


Figure 4. An example of equilibration in the reaction between CH_3O_2 and NO_2 at 353 K and 400 Torr total pressure, N_2 , and $[\text{NO}_2] = 9.58$ mTorr. The pre-trigger signal is equal to zero and is not shown. The fit is from global analysis.

T / K	$10^{12} k_1 / \text{cm}^3 \text{s}^{-1}$	k_1 / s^{-1}	$10^{14} K_c / \text{cm}^3$ Leeds	$10^{14} K_c / \text{cm}^3$ Bridier et al. ⁵
333	1.23 ± 0.10	32.3 ± 4.0	3.8 ± 0.6	4.6
343	1.66 ± 0.17	95 ± 9	1.70 ± 0.24	1.8
353	1.30 ± 0.16	207 ± 22	0.63 ± 0.10	0.72
363	0.92 ± 0.13	446 ± 46	0.21 ± 0.04	0.31

Table 2. Forward and reverse rate coefficients determined from $\text{CH}_3\text{O}_2 + \text{NO}_2$ at a total pressure of 400 Torr, N_2 . Errors are 2σ .

The enthalpy change for reaction 1, $\Delta_r H^\ominus_T(1)$, can be obtained at each temperature from the equilibrium constants in Table 2 by calculating the entropy change of reaction 1, i.e. using the third law method. A superior approach is described in the following sections. The analysis is based on a global fit to all the kinetic data (association and dissociation rate constants obtained under irreversible and equilibration conditions, reported here and in the literature), using the master equation program MESMER,³² which has the feature of non-linear least squares fitting.

All the $k_1(T)$ data in the temperature range 298 – 223 K from the studies of Sander et al., Ravishankara et al. and Bacak et al.^{3, 4 #18, 44} were used together with the decomposition data, k_1 , from Zabel et al.⁷ and Bridier et al.⁵ The total number of experimental values used in the fits was 63. The vibrational and rotational constants for each species were obtained from either experiment or the B3LYP/6-31+G** level of theory⁴⁷ and the newly formed bond RO₂—NO₂ was treated as a hindered rotor. The input parameters for this calculation are given in the SI. Overall the data

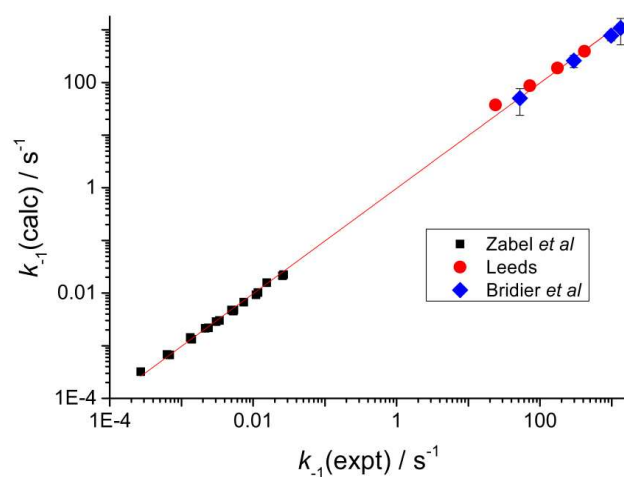


Figure 5. Plot of the experimental versus the MESMER calculated values for k_1 . The high values are from this study (●) and Bridier et al.⁵ (◆) and the low values (■) are from the nitrate decomposition studies of Zabel et al.⁷ The slope is equal to 1.007 ± 0.012 , which indicates exceptional agreement.

are in excellent agreement as shown in Figure 5, which is a correlation plot for the experimental and calculated rate constants. The final results for the best fit parameters are given in Table 3.

Figure 5 emphasises the strength of the master equation approach. It compares the calculated rate coefficients, obtained with the best fit parameters, with the experimental values under the same conditions of T and p. It includes the measurements made by Zabel et al.⁷ at low temperatures (253 – 272 K) and a range of pressures, and those obtained at higher temperatures and under equilibrating conditions by Bridier et al.⁵ (333 – 373 K, 760 Torr) and in this paper (333 – 363 K, 400 Torr). The rate coefficients cover a wide dynamic range (six orders of magnitude). The best fit line in Figure 5, constrained to pass through the origin, has a slope of 1.007 ± 0.012 , demonstrating the quality of the fit and the compatibility of the whole dissociation dataset with the master equation model and the best fit parameters. A similar plot is shown in the SI for the association data, which cover a much more limited dynamic range, but again shown a good agreement between fitted and measured values across the wide range of conditions used. The figure in the SI also highlights the inconsistency of the data from Wallington et al.⁶ with the other data used in this master equation analysis. Note that the MESMER fitting protocol accommodates different third bodies with differing energy transfer parameters.

From Table 3 it can be seen that our value of $\Delta_r H_{298}^\ddagger(1)$, $-93.6 \pm 0.3 \text{ kJ mol}^{-1}$, is in excellent agreement with the value of $-92.7 \pm 2.0 \text{ kJ mol}^{-1}$ obtained by Bridier et al.⁵

The improved error on our $\Delta_r H_{298}^{\circ}(1)$ determination is a consequence of including most of the literature data in our analysis. The wide dynamic range of the k_1 data, deriving from the low T dissociation studies of Zabel ⁷ and the higher T data obtained under equilibration conditions is important in defining the enthalpy of reaction. Note that the quoted uncertainty is based on the MESMER fit and does not include contributions from uncertainties in the input parameters. The actual uncertainty is probably higher and has potential contributions from our description of the internal angular/rotational motions of the system.

The high pressure limiting rate coefficient, used to determine the microcanonical dissociation constants in the ME model, using inverse Laplace transformation, was parameterised in the form $k_1^{\infty}(T) = A \times (T/298)^n$. The best fit value for n is -0.83 ± 0.88 (Table 3), which indicates that the limiting reaction rate coefficient decreases significantly as the temperature is increased. This type of temperature dependence is general for many bimolecular reactions that have large rate coefficients at room temperature, and can be explained by a variational transition-state on a barrierless potential energy surface (PES). ⁴⁸

Parameter	Value	Units
$\Delta_r H_0^{\circ}(1)$	-90.7 ± 0.2	kJ mol^{-1}
$\Delta_r H_{298}^{\circ}(1)$	-93.5 ± 0.3	kJ mol^{-1}
A: $k^{\infty} = A \times (T/298)^n$	$8.5 \pm 2.4 \times 10^{-12}$	$\text{cm}^3 \text{ molecule}^{-1} \text{ s}^{-1}$
n: $k^{\infty} = A \times (T/298)^n$	-0.83 ± 0.88	
$\Delta E_{\text{down},298}(\text{N}_2)$: $\Delta E_{\text{down},=}$	393 ± 110	cm^{-1}

$\Delta E_{\text{down},298} \times (T/298)^m$		
m: $\Delta E_{\text{down}} = \Delta E_{\text{down},298} \times (T/298)^m$	-0.10 ± 1.34	

Table 3. Master Equation fit to the $\text{CH}_3\text{O}_2 + \text{NO}_2$ data from this study together with that from the literature for both reactions (1) and (-1). The errors are $\pm 2\sigma$.

The most accurate way to parameterise the master equation results – $k_1(T,p)$ and $k_{-1}(T,p)$, in order to have an analytical representation is to use Chebyshev polynomials.⁴⁹ The Chebyshev polynomial coefficients can be calculated using MESMER and the coefficients are given in the SI. These polynomials provide the easiest way to regenerate the results of the master equation fits. In addition the master equation results were fitted to a Troe formalism and the parameters are given in the SI.

$\text{HO}_2 + \text{NO}_2 \rightarrow \text{HO}_2\text{NO}_2$

Four dissociation pathways are energetically possible upon photoexcitation of HO_2 at 248 nm:



It is generally accepted that photo-dissociation at wavelengths greater than 190 nm results solely in the $\text{OH} + \text{O}$ products.⁵⁰ Based on the above scheme, Hynes et al.⁵¹ developed a novel technique for the sensitive detection of the HO_2 using photolysis at

212 nm and detecting the OH photo-fragment a few ns later. In this study we are extending this technique by demonstrating that it can reliably measure rate coefficients, and also be used for a range of peroxy radicals.

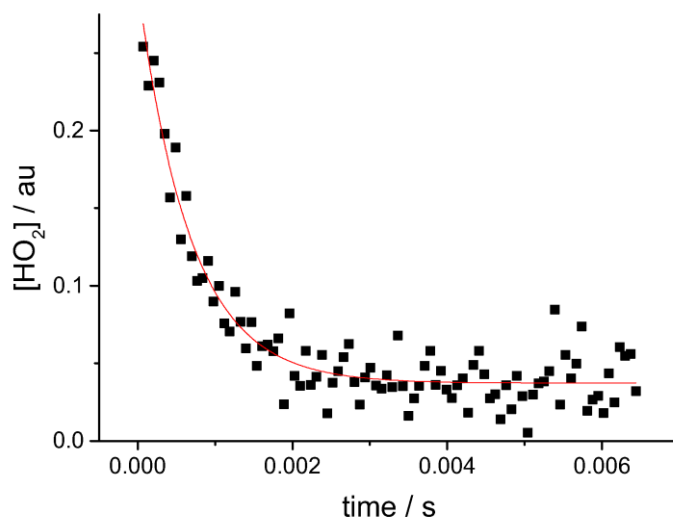


Figure 6. Kinetic trace showing the removal of HO₂ in the presence of NO₂ (=34.2 mTorr) at 400 Torr total pressure of N₂, $k_2' = 1478 \pm 100 \text{ s}^{-1}$. Note that at long times the signal does not return to zero, see text.

The three laser experiment using Cl / CH₃OH / O₂ to generate HO₂ - see experimental – generated an OH signal as a signature of HO₂. However, when the HO₂ photolysis laser was removed a significant OH signal was present at early times. To account for this OH signal, a three-laser and a two-laser experiment were recorded for each NO₂ concentration and the difference was assigned to HO₂. The source of OH in the two-laser experiment is most likely from:



Since $[\text{HO}_2] \gg [\text{OH}]$, only fraction of the HO₂ photolyses to OH, and OH is removed much faster in the system than HO₂, the subtraction procedure to determine the HO₂ decay is likely to be reliable; kinetic simulations further support this assertion. An example of an HO₂ kinetic trace at room temperature, obtained in this way, is shown

in Figure 6, where it is apparent that the concentration of HO₂ was found not to return to the pre-primary-photolysis zero. The origin of this behaviour will be discussed below.

Reaction 2 was studied over the pressure range 50 - 400 Torr at 295K, where nitrogen was the buffer gas, and up to 50 mTorr of NO₂ was added to the system. The data were fitted by the equation:

$$[\text{HO}_2] = [\text{HO}_2]_0 \exp(-k_2' t) + B \quad (\text{E2})$$

where k_2' is the pseudo-first-order rate constant, $k_2' = k_2[\text{NO}_2]$ and B is the non-zero long time signal. A modified and more detailed analysis, discussed below and in the SI, was used to determine k_2' . A typical bimolecular plot (k_2' vs $[\text{NO}_2]$) is shown in Figure 7 and the $k_2(p)$ data are plotted in Figure 8, together with the previous data from Sander et al.,¹³ Kurylo et al.,¹⁷ Christensen et al.¹⁸ and Bacak et al.¹⁹

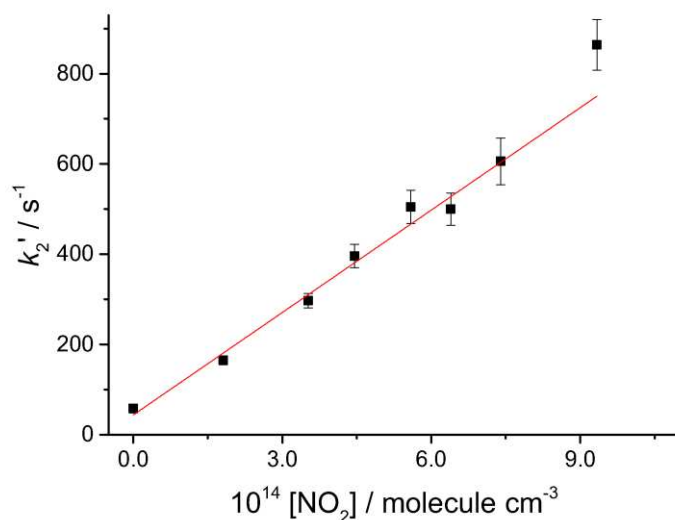


Figure 7. Bimolecular plot for the data for reaction 2 at 200 Torr at room temperature.

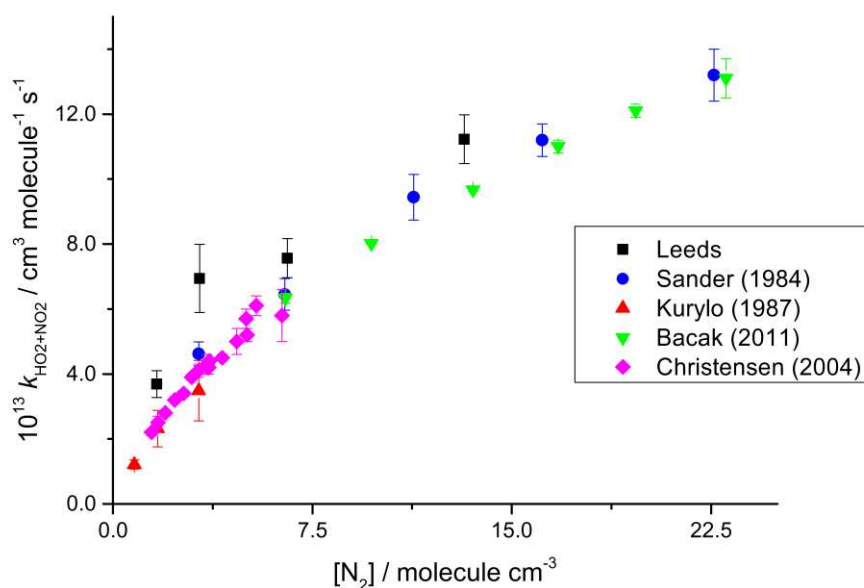


Figure 8. Plot of the pressure dependence of the bimolecular rate constant for reaction 2 at room temperature, where N₂ is the buffer gas: ■ = this study; ● = Sander et al.;³ ▲ = Kurylo et al.;¹⁷ and ▼ = Bacak et al.;⁴⁴ ◆ = Christensen et al.¹⁸ All errors are 2σ.

From Figure 8 it can be seen that our rate coefficients are within 30% of literature, but are generally on the high side. If this difference is from contributions to the HO₂ decay from HO₂ + NO then it requires our experiments to be photolysing ~2% of the NO₂. Based on the excimer laser fluence and NO₂ cross-section at 248 nm it is unlikely that there is this amount of photolysis. Also, the fact that our kinetic data on CH₃O₂ + NO₂ are in good agreement with the literature, see Figure 3, indicates there is little NO₂ photolysis. The effect of any NO₂ photolysis will, however be greater in the study of reaction 2, because k₂ is much smaller than k₁ (Figure 8 vs Figure 3). The more recent measurements by Christensen et al.¹⁸ and Bacak et al.¹⁹ used NIR and mass spectroscopy respectively to monitor HO₂ loss in the presence of NO₂. These higher precision studies reinforce the previous results of Kurylo et al.¹⁷ and Sander et al.¹³ at room temperature. Therefore we conclude that the present results are slightly high, even though the source of this discrepancy is not clear.

The accuracy associated with the present measurements mean that we have not pursued further kinetic removal measurements and instead have concentrated on the interpretation of the long-time residual signal, see Figure 6, and higher temperature experiments to observe equilibrium behaviour and attempt to determine the enthalpy of reaction.

Photolysis of HO₂NO₂ (PNA)

The residual OH signal observed at long time, see Figure 6, was typically 10% of [HO₂]₀. There are two possible sources of this observation: (i) thermal dissociation of PNA, regenerating HO₂ and NO₂ giving a steady state concentration of HO₂, or (ii) formation of OH in the photolysis of PNA. Lowering the temperature to 263K had no effect on the amount of residual OH signal indicating that thermal dissociation was not significant and that PNA photolysis was the source of OH:



It was possible, therefore, to obtain a quantum yield for the photolysis of PNA at 248nm by comparing the yields of OH on photolysis of HO₂ and of PNA. If all the HO₂ is removed by reaction with NO₂, which is not an unreasonable assumption as the first order rate coefficient for loss of HO₂ when [NO₂] = 0 is <50s⁻¹, then the following applies:

$$I_2 = C([\text{HO}_2] + X_2 [\text{HO}_2\text{NO}_2]) \quad \text{E3}$$

where C is a constant, I₂ = Intensity of OH fluorescence at time t and

$$X_2 = \frac{\text{Absorptioncross section of PNA} \times \phi_{\text{OH, PNA}}}{\text{Absorptioncross section of HO}_2 \times \phi_{\text{OH, HO}_2}}$$

Since the exponential increase in HO₂NO₂ has the same time constant as the decay of HO₂, then $I_2 = I_2^0(1 - X_2)\exp(-k_2't) + I_2^0 X_2$, which is in the same form as equation 2. Fits to the decay profiles give k_2' and X_2 . $\phi_{\text{OH,PNA}}$ can then be determined, assuming ϕ_{OH} from HO₂ photolysis is unity at 248nm.⁵⁰

$$\phi_{\text{OH,PNA}} = \frac{X_2 \sigma_{\text{HO}_2}}{\sigma_{\text{PNA}}}$$

The SI provides a more detailed analysis of equation E3, allowing for diffusive loss of HO₂ and PNA. In this solution, [HO₂] = M2, [HO₂NO₂] = M3 and k_{rev} (= k_2) and k_X (the thermal dissociation rate coefficient for PNA) are fixed to zero. Fitting the kinetic data using equation E3 yields X_2 and hence $\phi_{\text{OH,PNA}}$, as noted above.

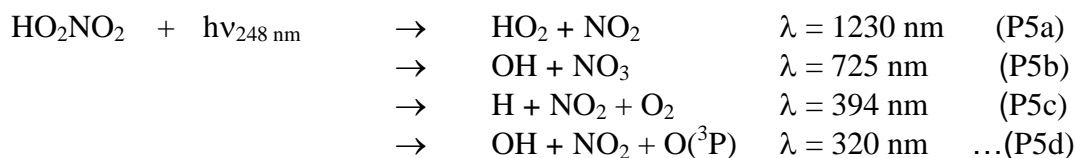
Data at 263 K were analysed globally using Origin – see above – where the data were fitted by the analytical expression for E3, as detailed in the SI. The values of X_2 and $\phi_{\text{OH,PNA}}$ are given in Table 4, together with previous determinations. Cross sections at 248nm were taken from JPL evaluation No. 16.⁵²

X_2 (Leeds)	0.086 ± 0.015
$\phi_{\text{OH, PNA}}$ (Leeds)	0.15 ± 0.03
$\phi_{\text{OH, PNA}}$ (Macleod et al.) ²²	0.34 ± 0.16
$\phi_{\text{OH, PNA}}$ (Jimenez et al.) ²⁴	0.085 ± 0.08
$\phi_{\text{HO}_2, \text{PNA}}$ (Jimenez et al.) ²⁴	0.89 ± 0.26
$\phi_{\text{OH, NO}_2}$ (Roehl et al.) ²³	0.56 ± 0.17

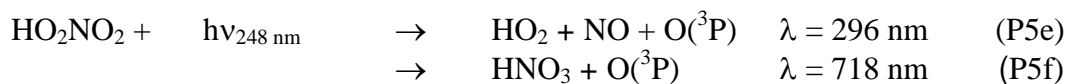
Table 4. Product yields from the photolysis of PNA at 248 nm. Errors are 2σ .

The previous study to measure the yield of the OH product yield from PNA photolysis by Macleod et al.²² determined $\phi_{\text{OH, PNA}} = 0.34 \pm 0.16$. In our experiments HO₂ is titrated with NO₂ to form PNA in time-resolved experiments where the chemistry is straightforward. However, in the experiments by Macleod et al.²² OH was measured from PNA relative to H₂O₂ where determinations of the absolute, unambiguous PNA concentrations were complicated by use of mass spectrometry. In addition, they assumed that the rotational distributions of OH after photolysis of PNA and H₂O₂ are the same. This might not necessarily be correct at the 5 / 40 mTorr of PNA/H₂O₂ and pump / probe delay time used in their study. More recently Jimenez et al.²⁴ determined $\phi_{\text{OH,PNA}} = 0.085 \pm 0.08$ at 248 nm by comparison to H₂O₂, where both the PNA and H₂O₂ concentrations were measured by FTIR. This result is in better agreement with the present study. This study and that of Jimenez et al.²⁴ are expected to be the more reliable determination of $\phi_{\text{OH,PNA}}$; the differences are within the combined uncertainties.

Roehl et al.²³ measured the quantum yield for NO₂ formation from the 248 nm photolysis of PNA and determined $\phi_{\text{NO}_2, \text{PNA}} = 0.56 \pm 0.17$ by comparison with HNO₃. If this result is combined with our PNA photolysis measurement then it might be concluded that:

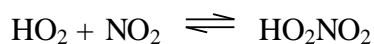


are not the only channels operating. Possible other channels include:



In the study of PNA photolysis Jimenez measured $\phi_{\text{HO}_2, \text{PNA}} = 0.89 \pm 0.26$.²⁴

Therefore it would appear that channel P4e is also operating in the 248 nm photolysis of PNA, but at longer wavelengths, relevant for atmospheric chemistry, only channel P4a is expected to be active.



The reaction between HO₂ and NO₂ was studied between 343 – 423 K and 400 Torr total pressure. Helium was the buffer gas in order to improve the data quality, (it does not quench the OH fluorescence) and hence increase the likelihood of observing equilibration in this reaction. Compared to the CH₃O₂ + NO₂ reaction, see Figure 4, equilibration was not apparent in the OH profiles, see Figure 9. The 10% baseline from PNA photolysis partially obscures any approach to equilibrium, but this should not prevent its observation. From a cursory inspection of the traces it appears that equilibrium was not present. However, upon closer inspection it is apparent that the

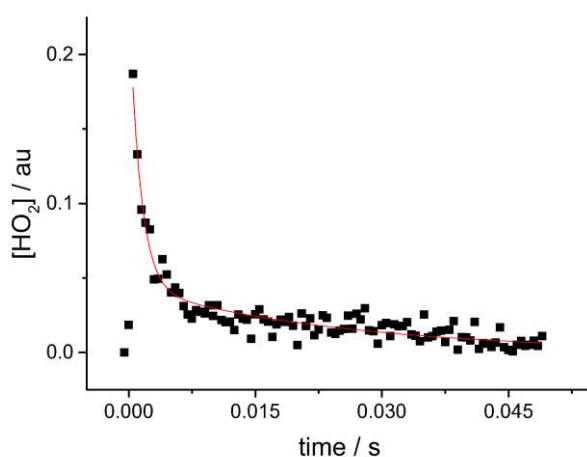


Figure 9. A decay trace showing the removal of HO₂ in the presence of 25.52 mTorr NO₂ at 393 K and a total pressure of 400 Torr. Biexponential behaviour is evident in this trace but analysis indicates that HO₂NO₂ is being lost via another channel, with rate constant k_X , as well as re-dissociation: $k_2' = 691 \pm 59 \text{ s}^{-1}$; $k_2 = 58 \text{ s}^{-1}$ (fixed); and $k_X = 42 \pm 3 \text{ s}^{-1}$; B was fixed at a value of 0.1.

traces were more complicated, because the equilibrated mixture decays much faster than was the case with CH_3O_2 (compare Figures 4 and 9).

These high temperature traces were analysed by fitting equation E3 to the data, where $k_2' = k_{\text{bim}}[\text{NO}_2]$, $k_2 = k_{\text{rev}}$, and k_{diff1} and k_{diff2} are the slow diffusion of HO_2 and HO_2NO_2 out of the reaction zone, and the baseline arising from PNA photolysis to OH was accounted for by fixing X_2 to the value given in Table 4, see SI for details of the fitting equation. The value of k_2 was fixed to the values given by the best fit parameters from the master equation; as will be discussed in a forthcoming paper. This analysis revealed that this model is an inadequate description of the data, and good fits are obtained only when an additional loss channel from HO_2NO_2 is added to the model.



The rate coefficient for this reaction is assigned k_X in the SI. k_X was observed to increase significantly with temperature and is comparable to k_2 , and this provides an explanation of why equilibrium is difficult to observe in this system. Attempts to float both k_X and to k_2 returned similar values but with very large error bars. The possibility that the product of reaction 14 is HONO has been studied by Dransfield et al.⁵³ and Tyndall et al.⁵⁴ Both found no evidence for this reaction occurring and Tyndall et al. placed an upper limit of $5 \times 10^{-16} \text{ cm}^3 \text{ molecule}^{-1} \text{ s}^{-1}$ on the second-order rate coefficient for reaction 14 at room temperature; it is unlikely that a highly uncompetitive channel can become competitive by 393 K. Alternatively, reaction 14 may involve the removal of PNA with the added reagents over the 343 – 423 K temperature range. Overall, these high temperature data show that additional reactions

are occurring in the system that prevent the unambiguous determination of independent values of k_2 and hence of the equilibrium constant.



Based on our detection of CH_3O from the 248 nm photolysis of CH_3O_2 it is expected that $\text{C}_4\text{H}_9\text{O}_2$ will produce $\text{C}_4\text{H}_9\text{O}$, which is known to fluoresce.⁵⁵⁻⁵⁶



However, when setting up this experiments, the hydroxyl radical, OH, was observed on the timescale consistent with $\text{C}_4\text{H}_9\text{O}_2$ kinetics. Experiments were also carried out using CH_3O_2 and OH was also detected that matched methyl peroxy kinetics. This observation is compatible with the observations of Hartmann who photolysed CH_3O_2 at 248 nm and assigned $\Phi_{\text{CH}_3\text{O}} = 0.2 \pm 0.1$ and $\Phi_{\text{OH}} = 0.06 \pm 0.03$.⁴⁰ The observation that $\text{C}_4\text{H}_9\text{O}_2$ is photolysed at 248 nm to produce OH is thus consistent with other studies of peroxy radical photochemistry:⁴⁰



This OH channel is more thermodynamically favourable than the butoxy channel and can occur at photolysis wavelengths out to the near IR.⁵⁷ Since OH is at least an order of magnitude more sensitive to detect than an alkoxy radical, the OH photo-fragment was used as the proxy for $\text{C}_4\text{H}_9\text{O}_2$ in the present study.

The reaction was initially studied at 241 and 268 K, temperatures at which there is no reverse reaction on the timescale of the experiments; all experiments were carried out at 100 Torr total pressure, helium.

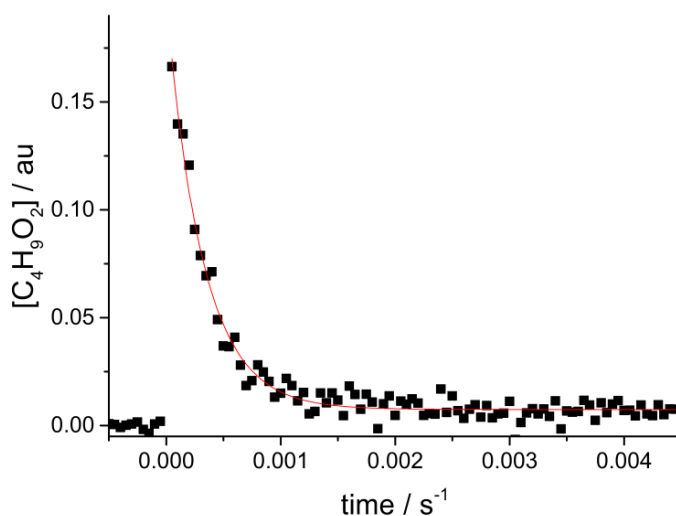


Figure 10. Kinetic trace of $C_4H_9O_2$ in the presence of NO_2 at 241 K and 100 Torr total pressure, helium. $[NO_2]$, $[O_2]$ $[Cl_2]$ and $[C_4H_{10}] = 4.75, 392, 97.0$ and 101.18 mTorr, respectively, and the removal rate constant k_3' is equal to $3150 \pm 108 \text{ s}^{-1}$.

The kinetic traces exhibited exponential decay but it was noted that the traces did not return to the pre-trigger baseline. Therefore, as for HO_2 , the data were fitted to the equation:

$$[C_4H_9O_2] = [C_4H_9O_2]_0 \exp(-k_3' t) + B \quad (E4)$$

where k_3' is the pseudo-first-order rate coefficient, $k_3' = k_3[NO_2]$ and B is the residual signal. This signal is most likely a result of $C_4H_9O_2NO_2$ photolysing to OH:



Photolysis of the product to OH was observed in the $HO_2 + NO_2$ reaction, see above.

Figure 10 is an example of a $C_4H_9O_2$ decay trace and shows that equation 4 is a good fit to the data and that at long times the signal has not returned to the baseline, $B > 0$.

This non-zero baseline makes it harder to observe equilibrium in reaction 3 at the higher temperatures. It needs to be quantified and fixed when analysing the higher temperature data. The data from reaction 3 is described by

$$I_3 = C'([C_4H_9O_2] + X_3 [C_4H_9O_2NO_2]) \quad E5$$

where I_3 = intensity of OH fluorescence at time t and

$$X_3 = \frac{\text{Cross section of BPN} \times \phi_{\text{OH}} \text{ BPN}}{\text{Cross section of HO}_2 \times \phi_{\text{OH}} \text{ HO}_2}$$

In the SI the analytical generic solution is given for equation E5, where $[\text{C}_4\text{H}_9\text{O}_2] = \text{M2}$ and $[\text{C}_4\text{H}_9\text{O}_2\text{NO}_2] = \text{M3}$. At 241 and 268 K only $k_3(k_{\text{bim}})$ and k_{diff1} (diffusion of $\text{C}_4\text{H}_9\text{O}_2$) are significant, so fitting of equation E5 to the data yields a defined value for X_3 . Global analysis was carried out on the data at each temperature using Origin in order to determine a more reliable value of k_3 and X_3 , see above for details. The results from this analysis are given in Table 5, where it can be seen that the non-zero baseline is well-defined by the low T experiments.

T / K	$10^{12} k_3 / \text{cm}^3 \text{ s}^{-1}$	X_3	k_3 / s^{-1}	$10^{13} Kc / \text{cm}^3$
241	11.7 ± 0.42	0.040 ± 0.004	na	
268	10.7 ± 0.62	0.040 ± 0.006	na	
293	6.49 ± 0.36	0.040 fixed	7.6 ± 7.2	8.54
316	7.68 ± 0.46	0.040 fixed	51.7 ± 9.8	1.49
341	5.48 ± 0.70	0.040 fixed	324 ± 30	0.17

Table 5. Returned parameters from the analysis of the $\text{C}_4\text{H}_9\text{O}_2 + \text{NO}_2$ data, errors are 2σ . All experiments were carried out at in 100 Torr of helium.

No change was observed in k_3 in experiments carried out at 400 Torr helium implying that the system is close to its high-pressure limit. Although no studies of 1-,2- $\text{C}_4\text{H}_9\text{O}_2$ have been made, these results are in reasonable agreement with the previous study of the reaction of t- $\text{C}_4\text{H}_9\text{O}_2$ with NO_2 ²⁵ that obtained a value of $1.2 \pm 0.3 \times 10^{-11} \text{ cm}^3 \text{ molecule}^{-1} \text{ s}^{-1}$ at 1 atmosphere of SF_6 . These observations indicate that reaction 3 is

close to its high-pressure limit, and this is tested in the master equation analysis discussed below.

At room temperature and above equilibration was observed. An example of equilibrium behaviour is shown in Figure 11, where it can be seen that the non-zero baseline is significantly larger than in Figure 10, indicating the approach to equilibrium with a non-zero concentration of the peroxy radical. In the analysis of this equilibration data X_3 was fixed to the value obtained at low temperatures, see Table 5, and k_3 and $k_{\text{diff}2}$ (diffusion of $\text{C}_4\text{H}_9\text{O}_2\text{NO}_2$) were assigned non-zero values in the fit. Global analysis was carried out for all the data at a given temperature in the same way as in the analysis of the $\text{CH}_3\text{O}_2 + \text{NO}_2$ data. The parameters returned from this analysis are given in Table 5.

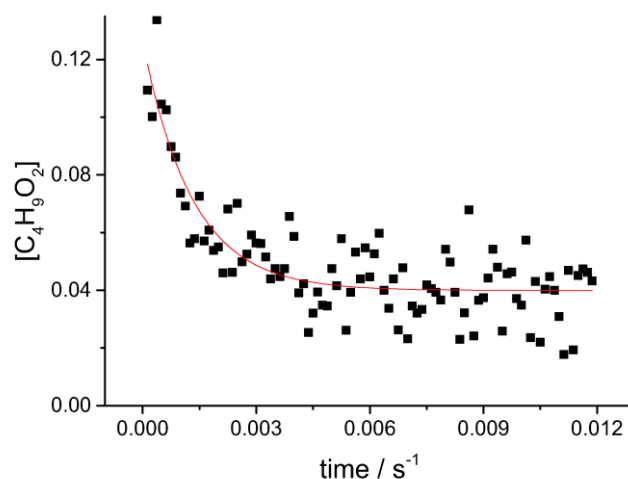


Figure 11. An example of equilibration in the reaction between $\text{C}_4\text{H}_9\text{O}_2$ and NO_2 at 341 K and 100 Torr total pressure, He, and $[\text{NO}_2] = 6.53 \text{ mT}$. The pre-trigger data are equal to zero and are not shown.

The enthalpy change for reaction 3, $\Delta_r H_0^\ominus(3)$, was determined in the same way as for reaction 1 by fitting a master equation model to the experimental data using MESMER. All the data in Table 5, together with the butyl nitrate decomposition

kinetic data of Zabel et al.,⁷ were used in this analysis, using the approach discussed in the master equation section. It is noted that Zabel et al.⁷ reacted chlorine atoms with n-butane to make the nitrate as used in this study. Therefore C₄H₉O₂NO₂ in both studies is mainly 2-C₄H₉O₂.³¹ All vibrational and rotational frequencies were calculated at the B3LYP/6-31+G** level of level of theory, the output frequencies were scaled by 0.96, and the newly formed bond, RO₂—NO₂, was treated as a hindered rotor. The input parameters for this calculation are given in the SI.

Overall the fit to the data is good but the amount of data is limited to that from this study, carried out in helium, and nitrate decomposition data carried out at just one temperature (253 K) and pressure (800 mBar, N₂). For this reason a temperature

Parameter	Value	Units
$\Delta_r H_0^\circ(3)$	-90.7 ± 0.3	kJ mol^{-1}
$\Delta_r H_{298}^\circ(3)$	-93.5 ± 0.3	kJ mol^{-1}
A: $k^\infty = A \times (T/298)^n$	$9.6 \pm 3.9 \times 10^{-12}$	$\text{cm}^3 \text{ molecule}^{-1} \text{ s}^{-1}$
n: $k^\infty = A \times (T/298)^n$	-0.60 ± 1.34	
$\Delta E_{\text{DOWN}}(\text{He})$	274 ± 126	cm^{-1}
$\Delta E_{\text{DOWN}}(\text{N}_2)$	799 ± 13926	cm^{-1}

Table 6. Master Equation fit to the C₄H₉O₂ + NO₂ data in this study together with the literature k_1 .⁷ The errors are 1σ .

independent ΔE_{down} , was used in the analysis and the results are given in Table 6. The master equation analysis showed that the system is close to but not at its high-pressure limit. This is the reason why the value of ΔE_{down} for N₂ is undefined with only one pressure point.

From Table 6 it can be seen that our value of $\Delta_r H^\circ_0(3)$ is equal to the value for reaction 1. Also from Table 6 it can be seen that the high pressure limit for reaction 3 has a negative temperature dependent rate coefficient, although the uncertainty is considerable. The temperature dependence is similar to that of reaction 1. In the SI the Master Equation results for $k_3(T,p)$ and $k_{-3}(T,p)$ are given in parameterised forms through Chebyshev coefficients and Troe parameters.

Conclusions

The application of a three-laser technique has been successfully demonstrated in a study of the kinetics of HO_2 , CH_3O_2 and 1-,2- $\text{C}_4\text{H}_9\text{O}_2$ with NO_2 . The peroxy radical was probed by pulsed photolysis with detection of the photo-fragment within a few 100 ns via laser induced fluorescence. The observation of a photolysis channel forming OH for 1-,2- $\text{C}_4\text{H}_9\text{O}_2$ means that this method may be applicable to other stable peroxy species by detection of the relevant alkoxy radical or OH.

- The kinetics and thermodynamics for the reaction CH_3O_2 with NO_2 were determined over the temperature range 295 - 363 K and 25 - 400 Torr of nitrogen. The values of the rate coefficient, $k_1(p)$, at room temperature are in excellent agreement with the literature values. Above room temperature equilibrium kinetics were observed. These data together with the literature data for the forward and reverse kinetics were analysed using a master equation methodology, using the code MESMER. This returned a high precision value for the enthalpy of reaction, $\Delta_r H^\circ_{298}(1)$, of $-93.5 \pm 0.3 \text{ kJ mol}^{-1}$ which is in good agreement with a

previous determination of -92.7 ± 2.0 kJ. The uncertainty is much reduced because of the use of the fitting routine in MESMER to analyse all available data, for both association and dissociation reactions, regardless of the pressure and temperature conditions used in their determination.

- The rate constants for reaction 2, $\text{HO}_2 + \text{NO}_2$, at 295 K were within 30% of those from previous studies, but appear a little high.
- The decay profiles of HO_2 in the presence of NO_2 are characterised by a non-zero baseline. This result is best interpreted as photolysis of the reaction product HO_2NO_2 , PNA, to OH. Analysis of the baseline data leads to $\phi_{\text{OH, PNA}} = 0.15$, in agreement with a recent study.
- Equilibrium in the reaction $\text{HO}_2 + \text{NO}_2$ was obscured by an additional loss channel from HO_2NO_2 that became significant at $T > 340$ K.
- Reaction 3, 1-,2- $\text{C}_4\text{H}_9\text{O}_2 + \text{NO}_2$, was studied between 100 and 400 Torr total pressure of helium and between 243 and 343 K. Reaction 3 was found to be close to its high-pressure limit rate coefficient, k_3^∞ , $9.6 \pm 3.9 \times 10^{-12} \text{ cm}^3 \text{ molecule}^{-1} \text{ s}^{-1}$. Equilibrium kinetics were observed at room temperature and above, and master equation analysis of these data and nitrate decomposition data returned $\Delta_r H_{298}^\circ(3) = -93.5 \pm 0.3 \text{ kJ mol}^{-1}$.

Acknowledgements

We thank Dr Branko Ruscic for helpful discussions on the thermochemistry of the reactions studied and Dr Robin Shannon for providing the rotational constants and vibrational frequencies of the species in reaction 3. We are grateful to NERC for funding (NE/K005820/1).

Supporting Information Available

The supporting information contains:

1. Global analysis of kinetic traces under equilibrating conditions, describing how the traces were fitted and the rate coefficients obtained.
2. Comparison of modelled and measured rate coefficients for k_1
3. Representations of $k(p,T)$ for $\text{RO}_2 + \text{NO}_2$ using Chebyshev polynomials and a Troe representation. The section describes the method used and gives parameters for both methods for the reactions studied.
4. Input parameters for the MESMER master equation analysis.
5. Chebyshev polynomials for calculating $k(p,T)$ for $\text{RO}_2 + \text{NO}_2$. A spreadsheet is provided as a separate Supporting Information file to facilitate use of the Chebyshev polynomials. The instructions for using the spreadsheet to calculate $k(p,T)$ under any conditions within the fitted range are given in the spreadsheet in Supporting Information II.

This information is available free of charge via the Internet at <http://pubs.acs.org>.

References

1. Nielson, T.; Samuelsson, U.; Grennfelt, P.; Thomsen, E. L., Peroxyacetyl Nitrate in Long-Range Transported Polluted Air. *Nature (London)* **1981**, 293, 553-555.
2. Cox, R. A.; Derwent, R. G.; Hutton, A. J. L., Significance of Peroxynitric Acid in Atmospheric Chemistry of Nitrogen Oxides. *Nature (London)* **1977**, 270, 328-329.
3. Sander, S. P.; Watson, R. T., Kinetics Studies of the Reactions of Methylperoxy with Nitric Oxide, Nitrogen Dioxide, and Methylperoxy at 298 K. *J. Phys. Chem.* **1980**, 84, 1664-1674.
4. Ravishankara, A. R.; Eisele, F. L.; Wine, P. H., Pulsed Laser Photolysis-Long Path Laser Absorption Kinetics Study of the Reaction of Methylperoxy Radicals with Monomeric Nitrogen Dioxide. *J. Chem. Phys.* **1980**, 73, 3743-3749.
5. Bridier, I.; Lesclaux, R.; Veyret, B., Flash Photolysis Kinetic Study of the Equilibrium Methylperoxy + Nitrogen Dioxide. *Chem. Phys. Lett.* **1992**, 191, 259-263.
6. Wallington, T. J.; Nielsen, O. J.; Sehested, K., Kinetics of the Reaction of CH_3O_2 Radicals with NO_2 . *Chem. Phys. Lett.* **1999**, 313, 456-460.
7. Zabel, F.; Reimer, A.; Becker, K. H.; Fink, E. H., Thermal Decomposition of Alkyl Peroxynitrates. *J. Phys. Chem.* **1989**, 93, 5500-5507.
8. Cox, R. A.; Patrick, K., Kinetics of the Reaction $\text{HO}_2 + \text{NO}_2(+\text{M}) = \text{HO}_2\text{NO}_2$ using Molecular Modulation Spectrometry. *Int. J. Chem. Kinet.* **1979**, 11, 635-648.
9. Howard, C. J., Kinetics of the Reaction of Hydroperoxy with Nitrogen Dioxide. *J. Chem. Phys.* **1977**, 67, 5258-5263.
10. Jemi-Alade, A. A.; Thrush, B. A., Reactions of Hydroperoxy with Nitric Oxide and Nitrogen Dioxide Studied by Mid-Infrared Laser Magnetic Resonance. *J. Chem. Soc., Faraday Trans.* **1990**, 86, 3355-3363.
11. Levine, S. Z.; Uselman, W. M.; Chan, W. H.; Calvert, J. G.; Shaw, J. H., The Kinetics and Mechanism of the Hydroperoxy-Nitrogen Dioxide Reactions; the Significance of Peroxynitric Acid Formation in Photochemical Smog. *Chem. Phys. Lett.* **1977**, 48, 528-535.
12. Morrison, B. M., Jr.; Hecklen, J., The Free Radical Oxidation of Formaldehyde in the Presence of Nitrogen Oxide (NO_2 and NO). *J. Photochem.* **1981**, 15, 131-145.
13. Sander, S. P.; Peterson, M. E., Kinetics of the Reaction Peroxyhydroxyl (HO_2) + Nitrogen Dioxide + M \rightarrow Pernitric Acid (HO_2NO_2) + M. *J. Phys. Chem.* **1984**, 88, 1566-1571.
14. Simonaitis, R.; Hecklen, J., Temperature Dependence of the Reactions of Hydroperoxy with Nitric Oxide and Nitrogen Dioxide. *Int. J. Chem. Kinet.* **1978**, 10, 67-87.
15. Zellner, R., Recombination Reactions in Atmospheric Chemistry. *Ber. Bunsenges. Phys. Chem.* **1978**, 82, 1172-1179.
16. Kurylo, M. J.; Ouellette, P. A., Pressure Dependence of the Rate Constant for the Reaction Hydroperoxy (HO_2) + Nitrogen Dioxide + M \rightarrow Pernitric Acid (HO_2NO_2) + M (M = N_2 , O_2) at 298 K. *J. Phys. Chem.* **1986**, 90, 441-444.
17. Kurylo, M. J.; Ouellette, P. A., Rate Constants for the Reaction Hydroperoxy Radical + Nitrogen Dioxide + Nitrogen \rightarrow Pernitric acid + Nitrogen: the Temperature Dependence of the Falloff Parameters. *J. Phys. Chem.* **1987**, 91, 3365-3368.

18. Christensen, L. E.; Okumura, M.; Sander, S. P.; Friedl, R. R.; Miller, C. E.; Sloan, J. J., Measurements of the Rate Constant of $\text{HO}_2 + \text{NO}_2 + \text{N}_2 \rightarrow \text{HO}_2\text{NO}_2 + \text{N}_2$ Using Near-Infrared Wavelength-Modulation Spectroscopy and UV-Visible Absorption Spectroscopy. *J. Phys. Chem. A* **2004**, 108, 80-91.
19. Bacak, A.; Cooke, M. C.; Bardwell, M. W.; McGillen, M. R.; Archibald, A. T.; Huey, L. G.; Tanner, D.; Utembe, S. R.; Jenkin, M. E.; Derwent, et al., Kinetics of the $\text{HO}_2 + \text{NO}_2$ Reaction: On the Impact of New Gas-phase Kinetic Data for the Formation of HO_2NO_2 on HO_x, NO_x and HO_2NO_2 Levels in the Troposphere. *Atmos. Environ.* **2011**, 45, 6414-6422.
20. Zabel, F., Unimolecular Decomposition of Peroxynitrates. *Z. Phys. Chem. (Munich)* **1995**, 188, 119-142.
21. Gierczak, T.; Jimenez, E.; Riffault, V.; Burkholder, J. B.; Ravishankara, A. R., Thermal Decomposition of HO_2NO_2 (Peroxynitric Acid, PNA): Rate Coefficient and Determination of the Enthalpy of Formation. *J. Phys. Chem. A* **2005**, 109, 586-596.
22. MacLeod, H.; Smith, G. P.; Golden, D. M., Photodissociation of Pernitric Acid (HO_2NO_2) at 248 nm. *J. Geophys. Res., D: Atmos.* **1988**, 93, 3813-3823.
23. Roehl, C. M.; Mazely, T. L.; Friedl, R. R.; Li, Y.; Francisco, J. S.; Sander, S. P., NO_2 Quantum Yield from the 248 nm Photodissociation of Peroxynitric Acid (HO_2NO_2). *J. Phys. Chem. A* **2001**, 105, 1592-1598.
24. Jimenez, E.; Gierczak, T.; Stark, H.; Burkholder, J. B.; Ravishankara, A. R., Quantum Yields of OH, HO_2 and NO_3 in the UV Photolysis of HO_2NO_2 . *Phys. Chem. Chem. Phys.* **2005**, 7, 342-348.
25. Langer, S.; Ljungstroem, E.; Ellermann, T.; Nielsen, O. J.; Sehested, J., Pulse Radiolysis Study of Reactions of Alkyl and Alkylperoxy Radicals Originating from Methyl tert-Butyl Ether in the Gas Phase. *Chem. Phys. Lett.* **1995**, 240, 499-505.
26. Melnik, D.; Miller, T. A., Kinetic Measurements of the $\text{C}_2\text{H}_5\text{O}_2$ Radical using Time-Resolved Cavity Ring-Down Spectroscopy with a Continuous Source. *J. Chem. Phys.* **2013**, 139, 094201/1-094201/18.
27. Robertson, S. H.; Glowacki, D. R.; Liang, C.-H.; Morley, C.; Shannon, R.; Blitz, M.; Tomlin, A.; Seakins, P. W.; Pilling, M. J. MESMER (Master Equation Solver for Multi-Energy Well Reactions), 2008-2013; an Object Oriented C++ Program Implementing Master Equation Methods for Gas Phase Reactions with Arbitrary Multiple Wells. <http://sourceforge.net/projects/mesmer>. (accessed 2015).
28. McKee, K. W.; Blitz, M. A.; Cleary, P. A.; Glowacki, D. R.; Pilling, M. J.; Seakins, P. W.; Wang, L., Experimental and Master Equation Study of the Kinetics of $\text{OH} + \text{C}_2\text{H}_2$: Temperature Dependence of the Limiting High Pressure and Pressure Dependent Rate Coefficients. *J. Phys. Chem. A* **2007**, 111, 4043-4055.
29. Blitz, M. A.; Hughes, K. J.; Pilling, M. J., Determination of the High-Pressure Limiting Rate Coefficient and the Enthalpy of Reaction for $\text{OH} + \text{SO}_2$. *J. Phys. Chem. A* **2003**, 107, 1971-1978.
30. Ghosh, B.; Papanastasiou, D. K.; Burkholder, J. B., Oxalyl Chloride, ClC(O)C(O)Cl : UV/Vis Spectrum and Cl atom Photolysis Quantum Yields at 193, 248, and 351 nm. *J. Chem. Phys.* **2012**, 137, 164315/1-164315/12.
31. Tyndall, G. S.; Orlando, J. J.; Wallington, T. J.; Dill, M.; Kaiser, E. W., Kinetics and Mechanisms of the Reactions of Chlorine Atoms with Ethane, Propane, and n-Butane. *Int. J. Chem. Kinet.* **1997**, 29, 43-55.
32. Glowacki, D. R.; Liang, C.-H.; Morley, C.; Pilling, M. J.; Robertson, S. H., MESMER: An Open-Source Master Equation Solver for Multi-Energy Well Reactions. *J. Phys. Chem. A* **2012**, 116, 9545-9560.

33. Pilling, M. J.; Robertson, S. H., Master equation models for chemical reactions of importance in combustion. *Annu. Rev. Phys. Chem.* **2003**, *54*, 245-275.
34. Miller, J. A.; Klippenstein, S. J., Master Equation Methods in Gas Phase Chemical Kinetics. *J. Phys. Chem. A* **2006**, *110*, 10528-10544.
35. Klippenstein, S. J.; Miller, J. A., From the Time-Dependent, Multiple-Well Master Equation to Phenomenological Rate Coefficients. *J. Phys. Chem. A* **2002**, *106*, 9267-9277.
36. Barker, J. R., Multiple-Well, Multiple-Path Unimolecular Reaction Systems. I. MultiWell Computer Program Suite. *Int. J. Chem. Kinet.* **2001**, *33*, 232-245.
37. Davies, J. W.; Green, N. J. B.; Pilling, M. J., The Testing of Models for Unimolecular Decomposition via Inverse Laplace Transformation of Experimental Recombination Rate Data. *Chem. Phys. Lett.* **1986**, *126*, 373-379.
38. Kenneth A. Holbrook; Michael J. Pilling; Robertson, S. H., *Unimolecular Reactions*, 2nd Edition. John Wiley & Sons: New York, 1996; p 434 pages.
39. Blitz, M. A.; Green, N. J. B.; Shannon, R. J.; Pilling, M. J.; Seakins, P. W.; Western, C. M.; Robertson, S. H., Reanalysis of Rate Data for the Reaction $\text{CH}_3 + \text{CH}_3 \rightarrow \text{C}_2\text{H}_6$ Using Revised Cross Sections and a Linearized Second-Order Master Equation. *J. Phys. Chem. A* **2015**, *119*, 7668-7682.
40. Hartmann, D.; Karthaeuser, J.; Zellner, R., The 248-nm Photofragmentation of the Peroxymethyl Radical. *J. Phys. Chem.* **1990**, *94*, 2963-2966.
41. Pilling, M. J.; Smith, M. J. C., A Laser Flash Photolysis Study of the Reaction Methyl + Molecular Oxygen \rightarrow Methylperoxy (CH_3O_2) at 298 K. *J. Phys. Chem.* **1985**, *89*, 4713-4720.
42. Atkinson, R.; Baulch, D. L.; Cox, R. A.; Crowley, J. N.; Hampson, R. F.; Hynes, R. G.; Jenkin, M. E.; Rossi, M. J.; Troe, J., *Evaluated Kinetic and Photochemical Data for Atmospheric Chemistry: Volume II - Gas Phase Reactions of Organic Species*. *Atmos. Chem. Phys.* **2006**, *6*, 3625-4055.
43. The MPI-Mainz UV/VIS Spectral Atlas of Gaseous Molecules of Atmospheric Interest. www.uv-vis-spectral-atlas-mainz.org (accessed 2015).
44. Bacak, A.; Bardwell, M. W.; Raventos-Duran, M. T.; Percival, C. J.; Hamer, P. D.; Shallcross, D. E., Kinetics of the $\text{CH}_3\text{O}_2 + \text{NO}_2$ Reaction: A Temperature and Pressure Dependence Study using Chemical Ionization Mass Spectrometry. *Chem. Phys. Lett.* **2006**, *419*, 125-129.
45. Beechem, J. M.; Knutson, J. R.; Brand, L., Global Analysis of Multiple Dye Fluorescence Anisotropy Experiments on Proteins. *Biochem Soc Trans* **1986**, *14*, 832-835.
46. Origin (OriginLab, Northampton, MA).
47. NIST Computational Chemistry Comparison and Benchmark Database. <http://cccbdb.nist.gov/> (accessed 2015).
48. Cleary, P. A.; Romero, M. T. B.; Blitz, M. A.; Heard, D. E.; Pilling, M. J.; Seakins, P. W.; Wang, L., Determination of the Temperature and Pressure Dependence of the Reaction $\text{OH} + \text{C}_2\text{H}_4$ from 200-400 K using Experimental and Master Equation Analyses. *Phys. Chem. Chem. Phys.* **2006**, *8*, 5633-5642.
49. Naik, C.; H.H. Carstensen; Dean, A. M. In *Reaction Rate Representation using Chebyshev Polynomials*, Spring Meeting of the Combustion Institute, San Diego, CA, San Diego, CA, 2002.
50. Langhoff, S. R.; Jaffe, R. L., Theoretical Study of the Four Lowest Doublet Electronic States of the Hydroperoxyl Radical: Application to Photodissociation. *J. Chem. Phys.* **1979**, *71*, 1475-1485.

51. Hynes, A. J.; Richter, R. C.; Nien, C. J., Laser Photofragmentation-Laser Induced Fluorescence Detection of the Hydroperoxyl Radical: Photofragment Energy Distributions, Detection Sensitivity and Kinetics. *Chem. Phys. Lett.* **1996**, 258, 633-638.
52. Sander, S. P.; Friedl, R. R.; Barker, J. R.; Golden, D. M.; Kurylo, M. J.; Wine, P. H.; Abbatt, J.; Burkholder, J. B.; Kolb, C. E.; Moortgat, G. K.; et al., Chemical Kinetics and Photochemical Data for Use in Atmospheric Studies Evaluation Number 16. JPL Publication 09-31: 2009.
53. Dransfield, T. J.; Donahue, N. M.; Anderson, J. G., High-Pressure Flow Reactor Product Study of the Reactions of HO_x + NO₂: The Role of Vibrationally Excited Intermediates. *J. Phys. Chem. A* **2001**, 105, 1507-1514.
54. Tyndall, G. S.; Orlando, J. J.; Calvert, J. G., Upper Limit for the Rate Coefficient for the Reaction HO₂ + NO₂ → HONO + O₂. *Environ. Sci. Technol.* **1995**, 29, 202-206.
55. Blitz, M.; Pilling, M. J.; Robertson, S. H.; Seakins, P. W., Direct Studies on the Decomposition of the tert-Butoxy Radical and its Reaction with NO. *Phys. Chem. Chem. Phys.* **1999**, 1, 73-80.
56. Jin, J.; Sioutis, I.; Tarczay, G.; Gopalakrishnan, S.; Bezant, A.; Miller, T. A., Dispersed Fluorescence Spectroscopy of Primary and Secondary Alkoxy Radicals. *J. Chem. Phys.* **2004**, 121, 11780-11797.
57. Frost, G. J.; Ellison, G. B.; Vaida, V., Organic Peroxyl Radical Photolysis in the Near-Infrared: Effects on Tropospheric Chemistry. *J. Phys. Chem. A* **1999**, 103, 10169-10178.

Figure Captions

Figure 1. Kinetic trace for $\text{CH}_3\text{O}_2 + \text{NO}_2$ at 295 K and 32.1 mTorr of NO_2 at 400 Torr total pressure. The solid line is the best fit first-order decay, E1, to the data, where $k_1' = 4505 \pm 421 \text{ s}^{-1}$.

Figure 2. Bimolecular plot for the $\text{CH}_3\text{O}_2 + \text{NO}_2$ kinetic data at a total pressure of 51 Torr (N_2) and at 295 K.

Figure 3. Plot of the pressure dependence of $\text{CH}_3\text{O}_2 + \text{NO}_2$ at 295 K from this study and the literature, where N_2 is the buffer gas: ■ = this study; ● = Ravishankara et al.;⁴ ▲ = Sander et al.;³ and ▼ = Bacak et al.⁴⁴ All errors are 2σ . The solid line is the MESMER fit to the data, see text below for details.

Figure 4. An example of equilibrium behaviour in the reaction between CH_3O_2 and NO_2 at 353 K and 400 Torr total pressure, N_2 , and $[\text{NO}_2] = 9.58 \text{ mT}$. The pre-trigger data is equal to zero and is not shown. The fit is from global analysis.

Figure 5. Plot of the experimental versus the MESMER calculated values for k_1 . The high values are from this study (●) and Bridier et al.⁵ (◆) and the low values (■) are from the nitrate decomposition studies of Zabel et al.⁷ The slope is equal to 1.007 ± 0.012 , which indicates exceptional agreement.

Figure 6. Kinetic trace showing the removal of HO_2 in the presence of NO_2 ($=34.2 \text{ mT}$) at 400 Torr total pressure, $k_2' = 1478 \pm 100 \text{ s}^{-1}$. Note that at long times the baseline does not return to zero, see text.

Figure 7. Bimolecular plot for the data for reaction 2 at 200 Torr at room temperature.

Figure 8. Plot of the pressure dependence of the bimolecular rate constant for reaction 2 at room temperature, where N_2 is the buffer gas: ■ = this study; ● = Sander et al.;³ ▲ = Kurylo et al.;¹⁷ and ▼ = Bacak et al.;⁴⁴ ◆ = Christensen et al.¹⁸ All errors are 2σ .

Figure 9. A decay trace showing the removal of HO_2 in the presence of 25.52 mTorr NO_2 at 393 K and a total pressure of 400 Torr. Biexponential behaviour is evident in this trace but analysis indicates that HO_2NO_2 is being lost via another channel, with rate constant k_X , as well as re-dissociation: $k_2' = 691 \pm 59 \text{ s}^{-1}$; $k_2 = 58 \text{ s}^{-1}$ (fixed); and $k_X = 42 \pm 3 \text{ s}^{-1}$; B was fixed at a value of 0.1.

Figure 10. Kinetic trace of $\text{C}_4\text{H}_9\text{O}_2$ in the presence of NO_2 at 241 K and 100 Torr total pressure, helium. $[\text{NO}_2]$, $[\text{O}_2]$, $[\text{Cl}_2]$ and $[\text{C}_4\text{H}_{10}] = 4.75, 392, 97.0$ and 101.18 mTorr , respectively, and the removal rate constant k_3' is equal to $3150 \pm 108 \text{ s}^{-1}$.

Figure 11. An example of equilibration in the reaction between $\text{C}_4\text{H}_9\text{O}_2$ and NO_2 at 341 K and 100 Torr total pressure, He, and $[\text{NO}_2] = 6.53 \text{ mT}$. The pre-trigger data are equal to zero and are not shown.

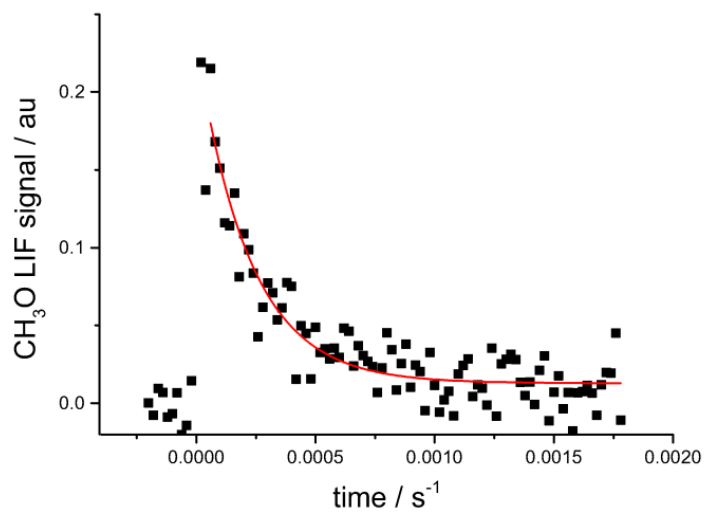


Fig. 1

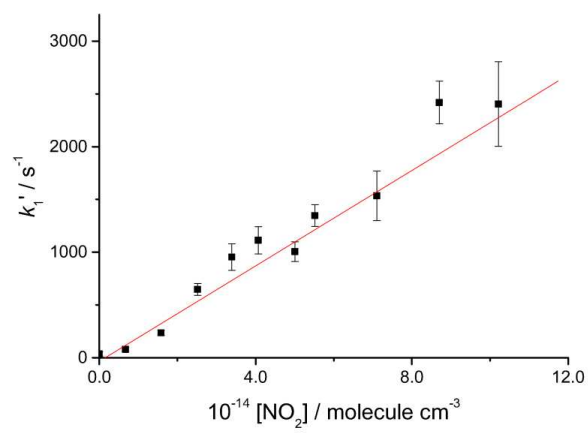


Fig. 2

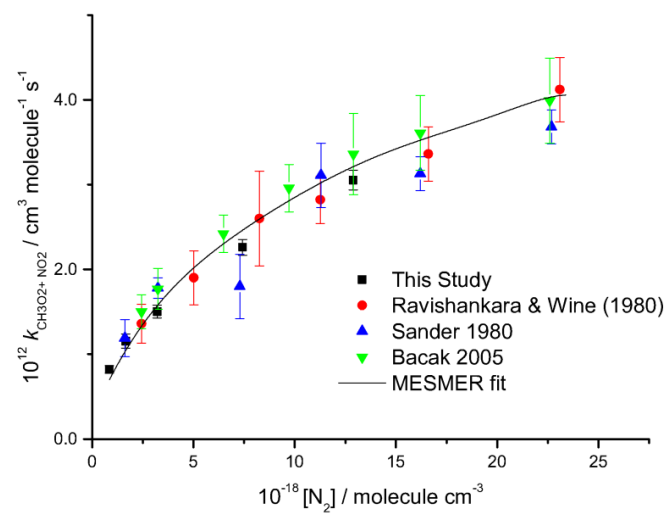


Fig. 3

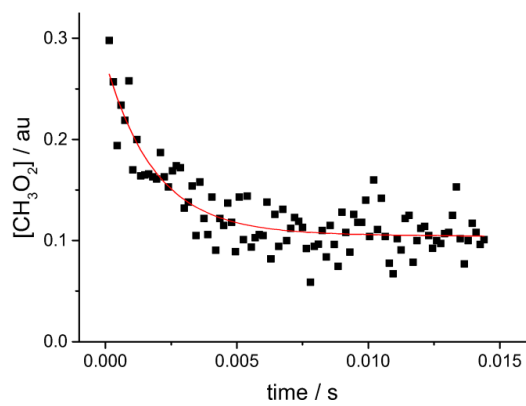


Fig. 4

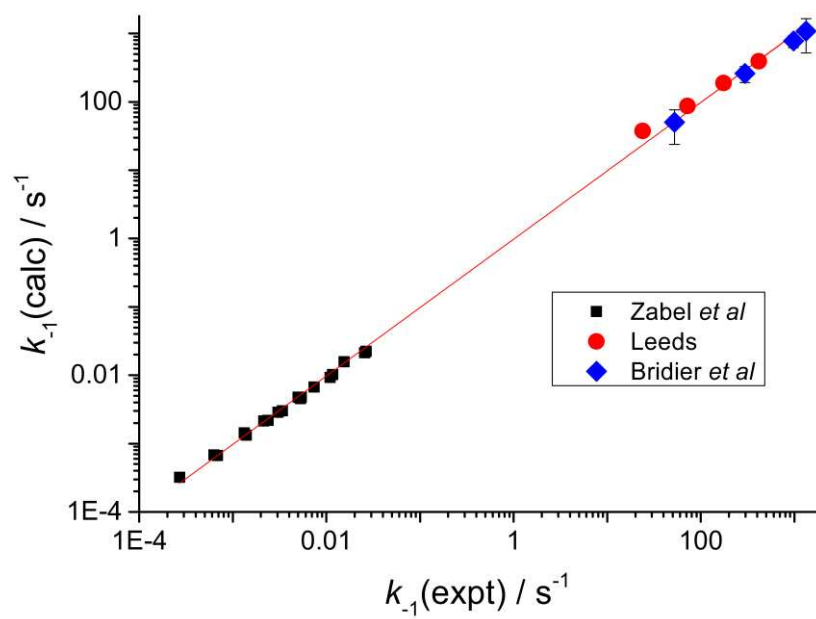


Fig. 5

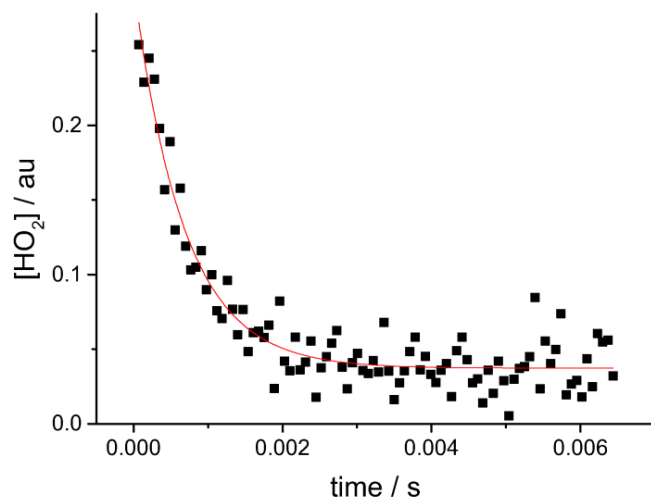


Fig. 6

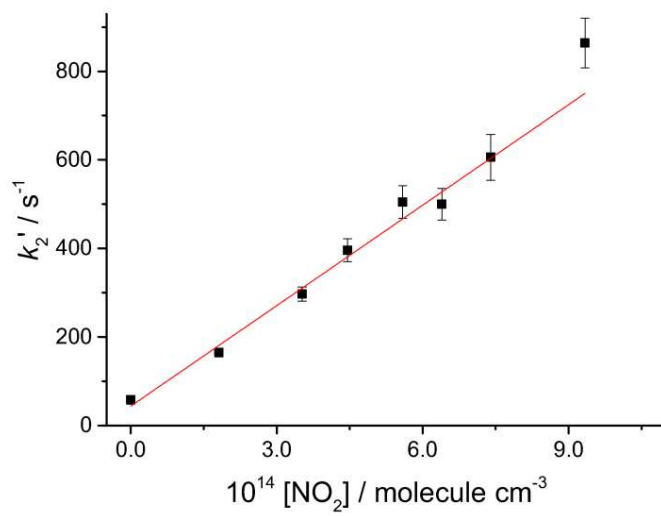


Fig. 7

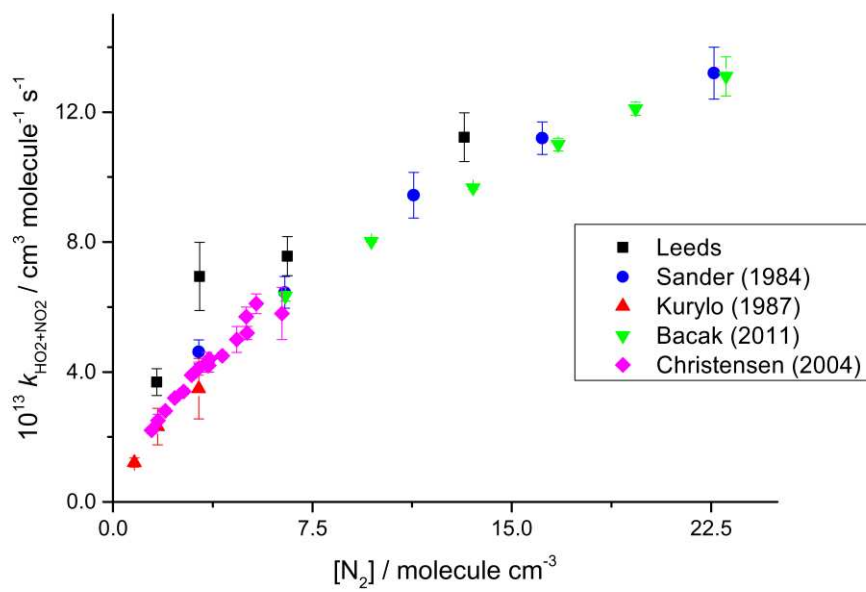


Fig. 8

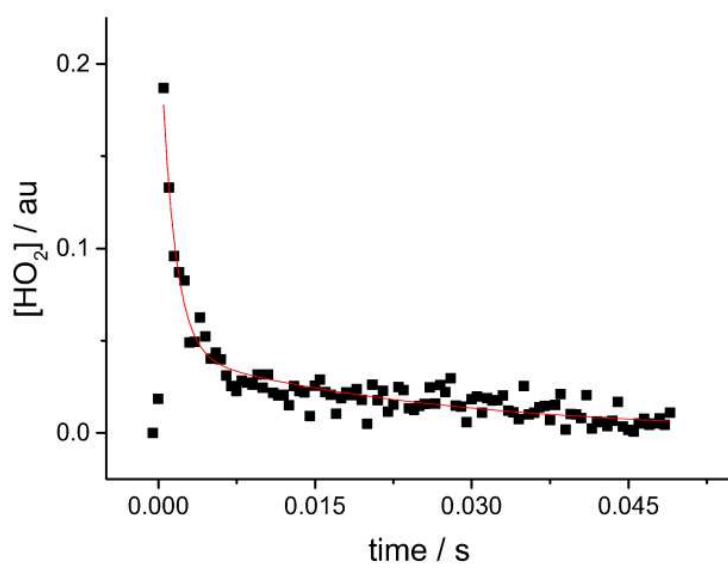


Fig. 9

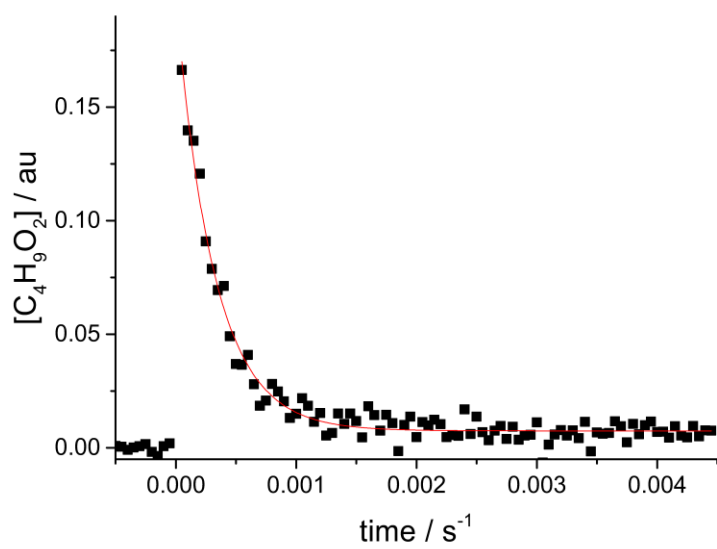


Fig. 10

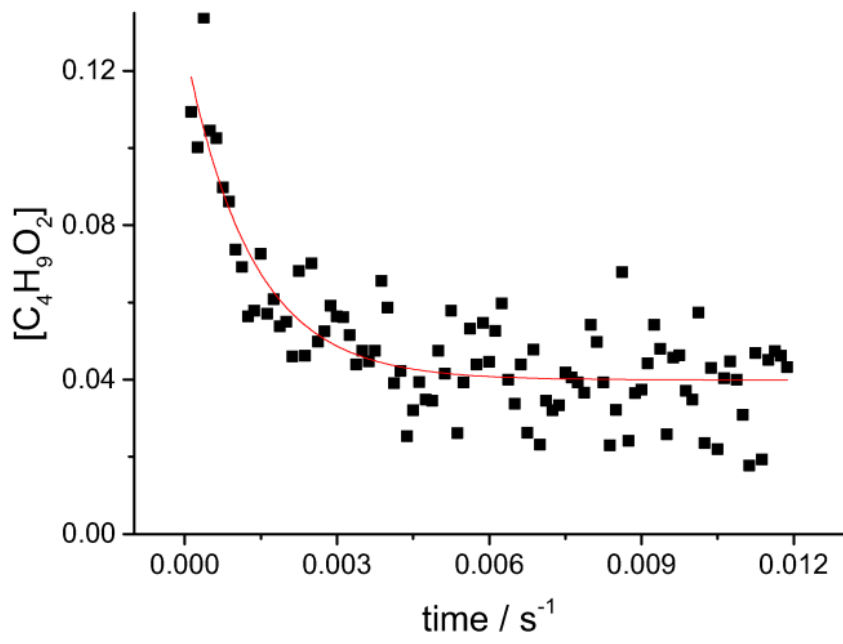


Fig. 11

TABLES

Pressure /Torr	$10^{12} k_1 / \text{cm}^3 \text{ molecule}^{-1} \text{ s}^{-1}$
26	0.82 ± 0.08
51	1.15 ± 0.16
99	1.50 ± 0.14
230	2.26 ± 0.18
399	3.05 ± 0.24

Table 1. Tabulated values of the bimolecular rate constant for $\text{CH}_3\text{O}_2 + \text{NO}_2$ at 295 K, with N_2 buffer gas. The errors are 2σ .

T / K	$10^{12} k_1 / \text{cm}^3 \text{ s}^{-1}$	k_{-1} / s^{-1}	$10^{14} K_c / \text{cm}^3$ Leeds	$10^{14} K_c / \text{cm}^3$ Bridier et al. ⁵
333	1.23 ± 0.10	32.3 ± 4.0	3.8 ± 0.6	4.6
343	1.66 ± 0.17	95 ± 9	1.70 ± 0.24	1.8
353	1.30 ± 0.16	207 ± 22	0.63 ± 0.10	0.72
363	0.92 ± 0.13	446 ± 46	0.21 ± 0.04	0.31

Table 2. Forward and reverse rate coefficients determined from $\text{CH}_3\text{O}_2 + \text{NO}_2$ at a total pressure of 400 Torr, N_2 . Errors are 2σ .

Parameter	Value	Units
$\Delta_r H^{\circ}_0(1)$	-90.7 ± 0.2	kJ mol^{-1}
$\Delta_r H^{\circ}_{298}(1)$	-93.5 ± 0.3	kJ mol^{-1}
A: $k^{\circ} = A \times (T/298)^n$	$8.5 \pm 2.4 \times 10^{-12}$	$\text{cm}^3 \text{ molecule}^{-1} \text{ s}^{-1}$
n: $k^{\circ} = A \times (T/298)^n$	-0.83 ± 0.88	
$\Delta E_{\text{down},298}(\text{N}_2)$: $\Delta E_{\text{down},=}$ $\Delta E_{\text{down},298} \times (T/298)^m$	393 ± 110	cm^{-1}
m: $\Delta E_{\text{down},=}$ $\Delta E_{\text{down},298} \times$ $(T/298)^m$	-0.10 ± 1.34	

Table 3. Master Equation fit to the $\text{CH}_3\text{O}_2 + \text{NO}_2$ data in this study together with the literature, both (1) and (-1). The errors are 2σ .

X_2 (Leeds)	0.086 ± 0.015
$\phi_{\text{OH, PNA}}$ (Leeds)	0.15 ± 0.03
$\phi_{\text{OH, PNA}}$ (Macleod et al.) ²²	0.34 ± 0.16
$\phi_{\text{OH, PNA}}$ (Jimenez et al.) ²⁴	0.085 ± 0.08
$\phi_{\text{HO}_2, \text{PNA}}$ (Jimenez et al.) ²⁴	0.89 ± 0.26
$\phi_{\text{OH, NO}_2}$ (Roehl et al.) ²³	0.56 ± 0.17

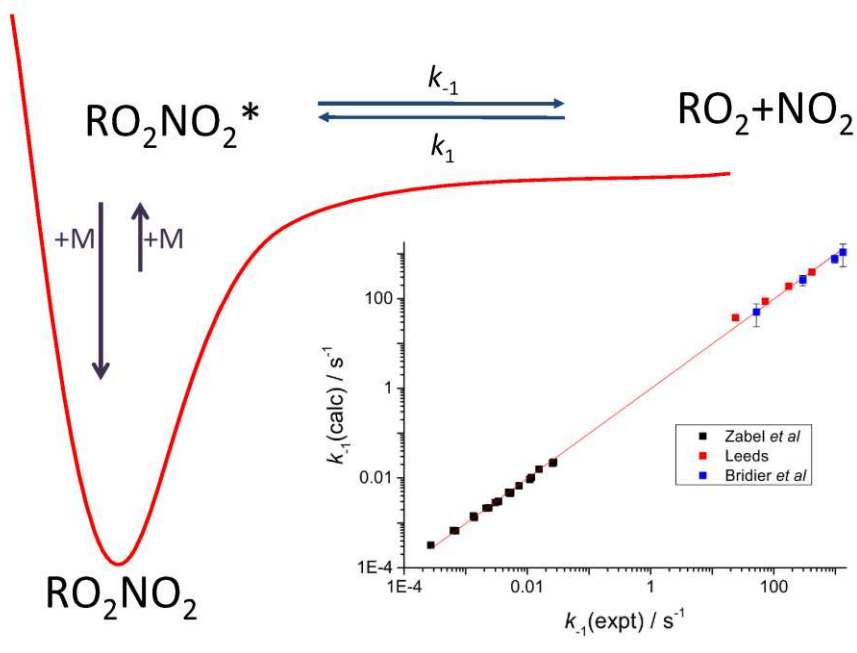
Table 4. Product yields from the photolysis of PNA at 248 nm. Errors are 2σ .

T / K	$10^{12} k_3 / \text{cm}^3 \text{ s}^{-1}$	X_3	k_3 / s^{-1}	$10^{13} Kc / \text{cm}^3$
241	11.7 ± 0.42	0.040 ± 0.004	na	
268	10.7 ± 0.62	0.040 ± 0.006	na	
293	6.49 ± 0.36	0.040 fixed	7.6 ± 7.2	8.54
316	7.68 ± 0.46	0.040 fixed	51.7 ± 9.8	1.49
341	5.48 ± 0.70	0.040 fixed	324 ± 30	0.17

Table 5. Returned parameters from the analysis of the $\text{C}_4\text{H}_9\text{O}_2 + \text{NO}_2$ data, errors are 2σ . All experiments were carried out at in 100 Torr of helium.

Parameter	Value	Units
$\Delta_r H^\circ_0(3)$	-90.7 ± 0.3	kJ mol^{-1}
$\Delta_r H^\circ_{298}(3)$	-93.5 ± 0.3	kJ mol^{-1}
A: $k^\infty = A \times (T/298)^n$	$9.6 \pm 3.9 \times 10^{-12}$	$\text{cm}^3 \text{ molecule}^{-1} \text{ s}^{-1}$
n: $k^\infty = A \times (T/298)^n$	-0.60 ± 1.34	
$\Delta E_{\text{DOWN}}(\text{He})$	274 ± 126	cm^{-1}
$\Delta E_{\text{DOWN}}(\text{N}_2)$	799 ± 13926	cm^{-1}

Table 6. Master Equation fit to the $\text{C}_4\text{H}_9\text{O}_2 + \text{NO}_2$ data in this study together with the literature k_1 .⁷ The errors are 1σ .



TOC graphic